Journal of Structural Geology, Vol. 6, No. 4, pp. 339 to 368, 1984
Printed in Great Britain

0191-8141/84 $03.00 + 0.00

Finite strain patterns and their significance in Permian rocks of the Alpes Maritimes (France)

A. W. B. SIDDANS,

Institut de Géologie, Université Louis Pasteur, F-67084 Strasbourg, France

B. HENRY,

Laboratoires de Tectonophysique et de Géomagnétisme, Université Pierre et Marie Curie, F-75230 Paris, France

R. KLIGFIELD,

Department of Geological Sciences, University of Colorado, Boulder, CO 80309, U.S.A.

W. LOWRIE and A. HIRT

Institut für Geophysik, E.T.H.-Hönggerberg, CH-8093 Zürich, Switzerland

and

M. N. PERCEVAULT

Centre Armoricain d'Etude Structurale des Socles, Université de Rennes, F-35042 Rennes, France

(*Received* 9 *December* 1982: *accepted in revised form* 13 *October* 1983)

Abstract—More finite strain data has been obtained from autochthonous Permian mudstones of the Alpes Maritimes, S.E. France. These new data were computed from field measurements of green spots on all available sections, deformed mudcracks and from the quantitative correlation between magnetic susceptibility anisotropy and finite strain in these rocks. Previously published finite strain data and the new results are presented on a series of structural maps and cross-sections for the Dôme de Barrot, the Tinée and Vionène region and the Roya region. As in previous studies difficulties arise in explaining the apparently variable extension parallel with the 100°, subhorizontal bedding–cleavage intersection: either this is real or there were large volume changes during the tectonic deformation. Study of quartz fibres, developed in deformed mudcracks in the Tinée valley, suggest that early in the tectonic history incremental stretching directions were parallel with the bedding–cleavage intersection, while later they were down-dip in the 100° trending cleavage. Since these Permian rocks have remained stuck to the Argentera basement they also record displacements and deformations in the basement. The early 100°, subhorizontal stretching is consistent with NW–SE dextral, strike-slip basement faulting, while later, down-dip stretching in the cleavage is consistent with contraction faults in the basement. This information and new palaeomagnetic data on the same samples are combined with recent geophysical evidence and regional tectonic studies, to provide a new precision to the tectonic history of this part of the Western Alpine External Zone.

INTRODUCTION

THE STUDY area is located in the southernmost parts of the Western Alpine External Zone (Fig. 1). Permian rocks and the Werfenian quartzites here constitute the autochthonous sedimentary cover of the crystalline basement massifs of Argentera and Maures–Esterel. Stratigraphically younger rocks have been detached at various levels in the Middle and Upper Trias, Jurassic and Cretaceous, displaced, faulted and folded to form the pseudo-cover of the Argentera Massif and Dôme de Barrot, the Tinée nappes and the Nice and Castellane Arcs (Fig. 1). North and east of the Argentera Massif the External Zone is overlain tectonically by units of more internal origin. Outline geologic maps and cross-sections (Figs. 1, 2 and 3) illustrate the regional structure. Alpine deformation of the Chaînes Subalpines in the External Zone is dated stratigraphically as Miocene–Pliocene, but in the southwest this is superposed on late Eocene structures of the Provençale phase (Goguel 1932, 1933). The distribution of structures of these two phases in Provence and the Chaînes Subalpines is illustrated by Goguel (1936, figs. 1, 248). Over-thrusting of the internal zones onto the External Zone was of late Oligocene age.

The Permian rocks are a discontinuous and heterogeneous series of continental redbeds, that accumulated in discrete basins. Palaeogeographic reconstructions (Faure-Muret 1955, fig. 30, pl. 3) show thickness variations from nearly zero to 3.5 km. Lower parts of the succession are largely conglomeratic and arkosic sandstones, the upper part (Série de Capeirotto) is predominantly pelitic and locally rich in mudcracks and green spots. The angular discordance at the base of the Werfenian quartzites was recognized by Faure-Muret (1948, 1955, pp. 193–195) as being due to a pre-Triassic period of deformation, the Palatine phase, marking the end of the Hercynian cycle. The Permian rocks now

SG 6:4-A

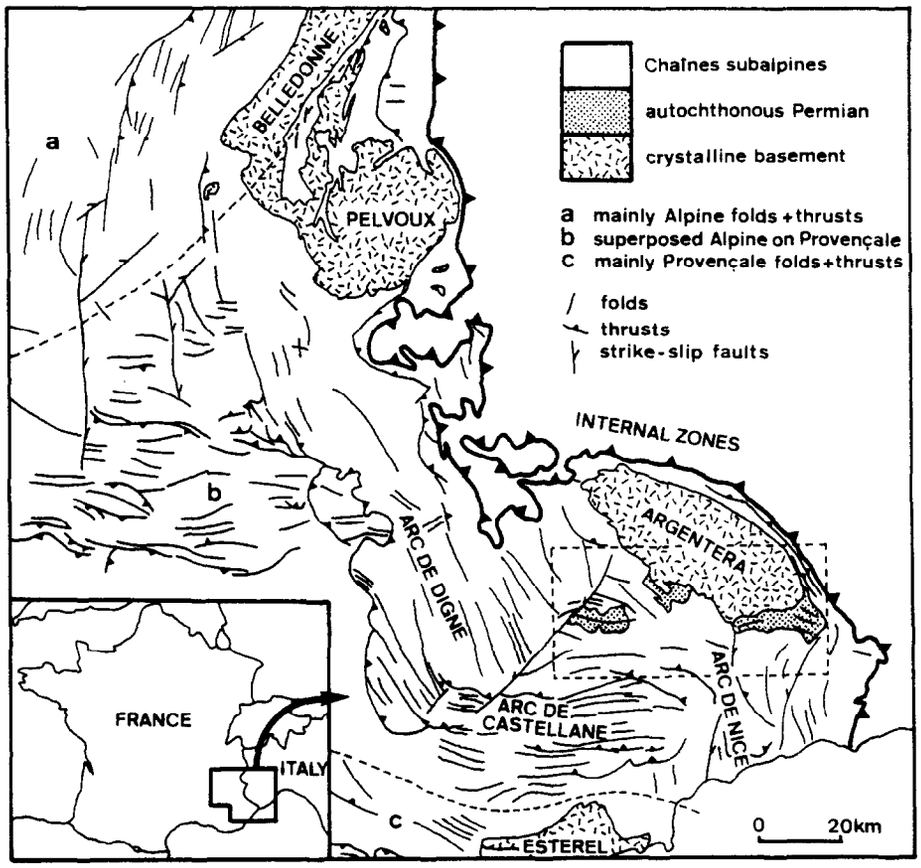

Fig. 1. Outline structural map of the southern External Zone of the Western Alps, showing location of the study area in the Alpes Maritimes (enclosed in broken lines). After Debelmas (1974, fig. 190a), Graham (1978a, fig. 2) and Siddans (1979, fig. 1).

outcrop in three main regions (Fig. 2), the Dôme de Barrot, a large domal structure, which the present day erosion level reveals as a window through the detached Mesozoic and Tertiary rocks; and along the southwest margin (Tinée valley, Vionène valley to Mt. Giraud) and southeast end (St. Martin–Vésubie to the Roya valley) of the Argentera Massif. The geology of these regions is described in detail by Goguel (1936), Bordet (1950) and Henry (1971) for the Dôme de Barrot region, by Faure-Muret (1955), Vernet (1967a, b), Lanteaume (1968), Malaroda *et al.* (1970), Vaslet (1978), Bogdanoff (1980) and Graham (1981) for the Argentera Massif and its cover. Geologic maps, Puget-Théniers and St. Martin–Vésubie of the Carte de France, 1/50,000 and those by Lanteaume (1968), Malaroda *et al.* (1970) and Vaslet (1978), provide complete coverage of the area. The map by Ménard (1980, fig. 1), showing depth to the pre-Trias basement according to borehole and seismic data, includes the region between the Argentera and Maures–Esterel Massifs.

A number of interrelated problems seemed to merit further strain studies in the Permian rocks. From the purely strain analysis point of view:

(1) Previous studies (Graham 1978b, Siddans 1980, Kligfield *et al.* 1981a) leave unresolved problems concerning apparently variable extensions parallel with the bedding–cleavage intersection and volume changes.

(2) The quantitative correlation between anisotropy of magnetic susceptibility and finite strain in these redbeds (Kligfield *et al.* 1981a), provides a method of finite strain estimation that can be used where there are no natural strain markers. It is a rapid method that can be used to estimate strains around individual structures.

(3) New methods of strain integration and removal (Cobbold 1979, Cobbold & Percevault 1983) provide new tools in the interpretation of observed strain patterns.

From a regional structural evolution point of view:

(4) Since Faure-Muret (1947) described Alpine deformation of the crystalline basement, with Middle Trias limestones in synclines above zones of high deformation in the basement, it has been clear that several Alpine faults traverse the basement. The nature of these faults is less clear, some are demonstrably thrusts or reverse faults (Lemoine 1948, Vaslet *et al.* 1977, Graham 1978b, Bogdanoff 1980), others are NW–SE dextral, strike-slip faults (Vernet 1965, 1979, Horrenberger *et al.* 1978, Bogdanoff 1980). Patterns of finite and incremental strain in the Permian rocks should provide additional evidence about the nature of these faults.

(5) The magnitude of strains associated with the pre-Trias deformation and their relationship with basement structures remains uncertain (Graham 1978b, Siddans 1980).

From a palaeomagnetic point of view:

(6) The Permian rocks of the Dôme de Barrot are little

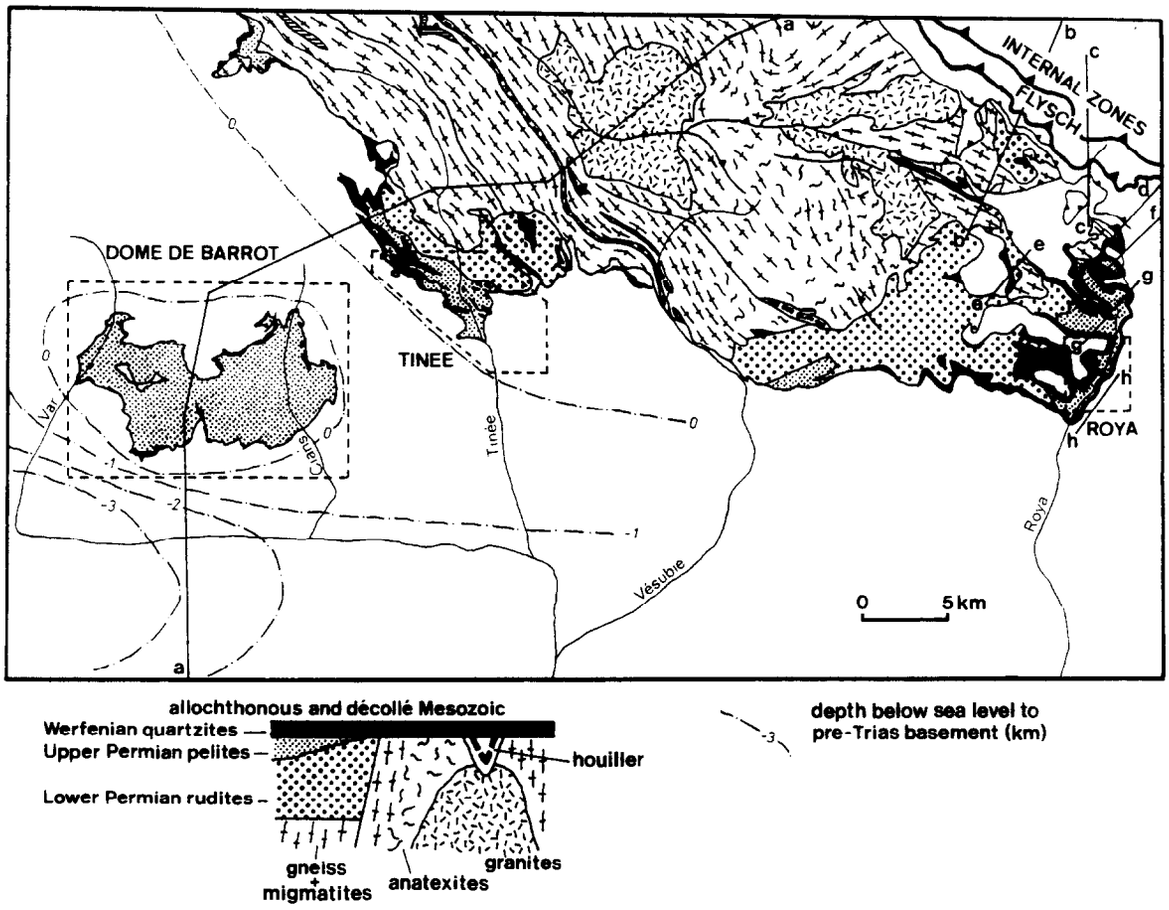

Fig. 2. Outline map of the Dôme de Barrot–Argentera Massif region, showing lines of cross sections in Fig. 3 and (enclosed in broken lines) the three sub-regions: Dôme de Barrot (Fig. 9), Tinée region (Figs. 12 and 13), Roya region (Fig. 18). After Bogdanoff (1980, fig. 3), Graham (1978b, fig. 13), Lanteaume (1968, pl. 2), Malaroda *et al.* (1970), Ménard (1980, fig. 1) and Vaslet *et al.* (1977, in Amaudric du Chaffaut & Villey 1979, fig. 3).

deformed or undeformed except for the effects of compaction. The remanent magnetization in these rocks records a stable palaeomagnetic direction with declination 208° and inclination −10° (Henry 1973, van den Ende 1970, 1977). This agrees with the palaeomagnetic results obtained in undisturbed Permian redbeds from the Esterel Massif (Zijderveld 1975). Bogdanoff & Schott (1977) studied the folded Permian rocks of the Tinée valley, Vésubie–Vallon de Graus and Roya valley regions. After applying a simple unfolding correction, but disregarding the distortional effects of internal deformation, they obtained a mean magnetization direction with declination 203° and inclination −21°. Recent investigations of deformed rocks from the Dôme de Barrot, Tinée and Roya valleys have given similar mean directions up to the triaxial strain stage of deformation (Kligfield *et al.* 1983). However, the directional scatter produced by internal distortion is unacceptably large beyond the appearance of 'pencil structure' deformation. Attempts to remove the effects of distortional strain by treating the remanent magnetization as a passive marker were unsuccessful beyond the 'pencil structure' stage, presumably because of a rheological change of the rock matrix resulting from recrystallization of illite and chlorite. For rocks that had suffered only compactional or 'pencil structure' strain, corrections to the remanence by the passive marker technique had insignificantly small effect on the mean directions.

FINITE STRAIN ANALYSIS

Previous studies

Graham (1978b) made the first systematic finite strain analyses in these Permian redbeds, from Rf/ϕ analysis of green spot shapes on naturally occurring principal planes. Tectonically undeformed mudstones were recognized in the south Daluis Gorges (Var river section, west Dôme de Barrot), which showed compactional strains of 40% flattening in the bedding, probably achieved by volume reduction. It was also suggested that a progressive tectonic deformation, more or less pure shear with a 0.03 incremental volume loss, having the tectonic shortening direction oriented about 010° horizontal and the tectonic extension direction about vertical, when superposed on the compactional strains, could largely explain the observed sequence of spot shapes (Graham 1978b, figs. 4 to 14):

(i) Oblate in bedding where there is no tectonic deformation (south Daluis Gorges).

(ii) Triaxial shapes with short axis, Z, normal to bedding and long axis, X, 100° subhorizontal in the bedding (north Daluis Gorges).

(iii) Prolate shapes with X oriented 100° subhorizontal in bedding, associated with pencil structure development parallel to X (north Cians Gorges, east Dôme de

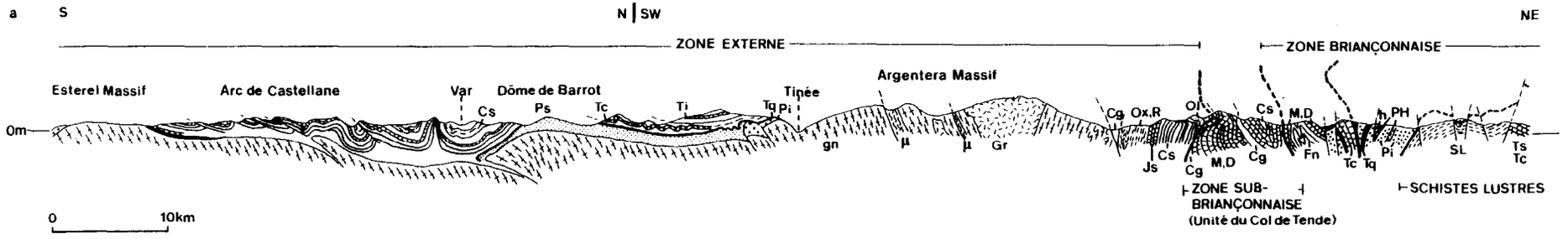

Fig. 3. Sections across the southern External Zone of the Western Alps showing the major structural geometry of the tectonic units and their relationship with the internal zones. See Fig. 2 for section lines. After: (a) Goguel (1936, pl. 2, section 5), Bordet (1950, fig. 11), Graham (1978b, figs. 2 and 3), Malaroda *et al.* (1970) and Ménard (1980, fig. 2); (*continued*)

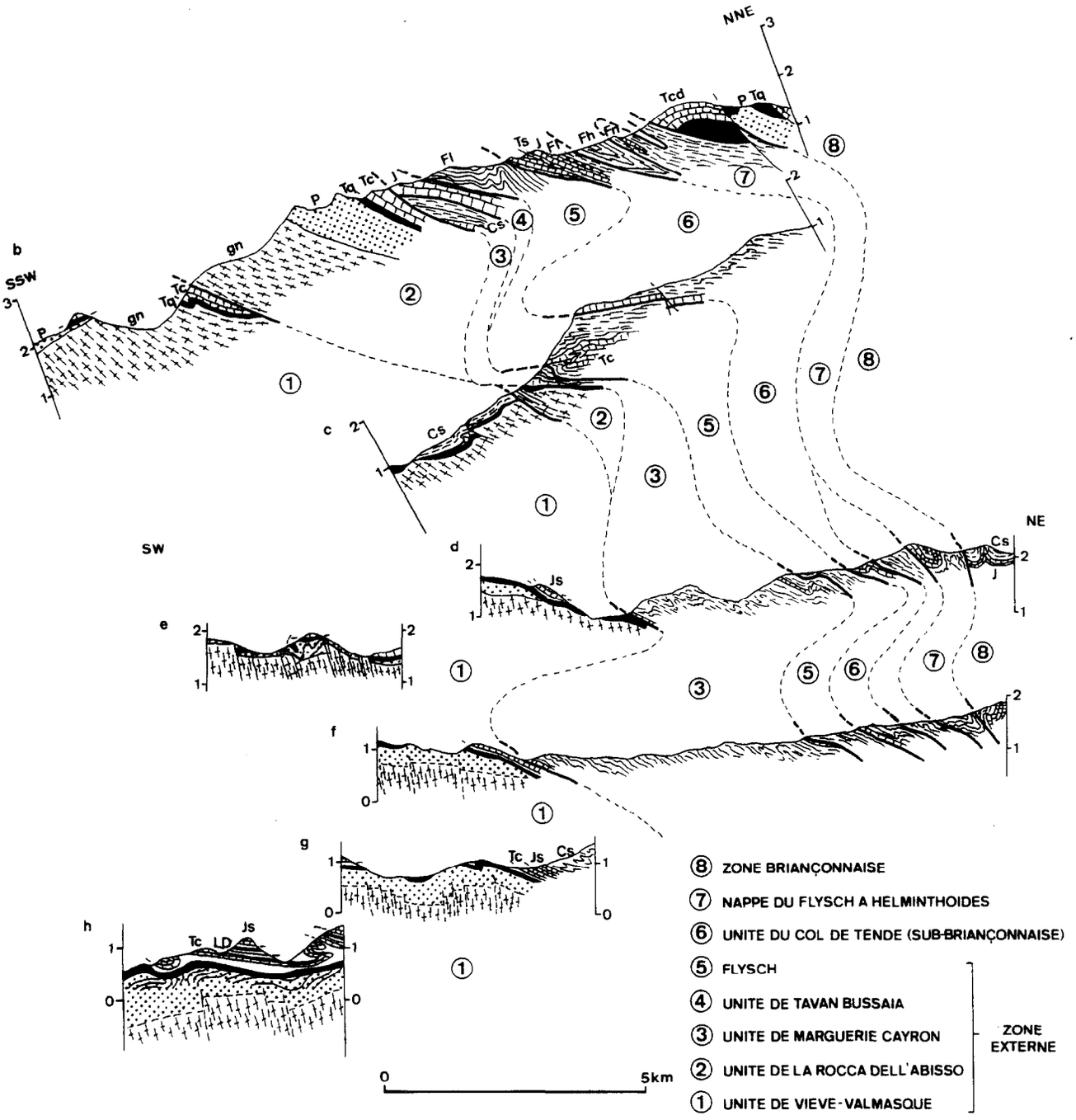

Fig. 3. (*continued*) After (b) Sturani (1967, fig. 17), Vernet (1967b, fig. 7), Faure-Muret & Fallot (1957, pl. 1); (c) Campredon & Boucarut (1975, fig. 92), Faure-Muret & Fallot (1957, fig. 1); (d) Lanteaume (1968, fig. 129); (e) Aicard *et al.* (1968, pl. 2); (f) Lanteaume (1968, fig. 129); (g) Lanteaume (1968, fig. 99); (h) Lanteaume (1968, fig. 100) and Graham (1978b, fig. 12).

Barrot and at the southern end of the Tinée valley section).

(iv) Triaxial shapes with Z oriented 010° and X oriented 100°, both subhorizontal in bedding (central Cians Gorges, southern parts of the Tinée section and in the Roya section).

(v) Oblate in cleavage with Z oriented 010° subhorizontal, normal to cleavage and approximately in bedding (central parts of the Tinée section).

(vi) Triaxial shapes with Z oriented 010° normal to cleavage and X parallel to the down-dip lineation in the cleavage (northern parts of the Tinée section, the Vionène valley and in northern parts of the Roya section).

Plotted on a logarithmic Flinn diagram (Graham 1978b, fig. 15), this sequence of spot shapes forms a characteristic pattern, which was suggested to be the deformation path followed by these rocks. This deformation path is shown here in Figs. 11, 15 and 20. It was also suggested that the geographic distribution of these strains (Graham 1978b, fig. 13) was due to the Permian rocks being 'nipped into' synclines above contraction faults in the basement, since the high strain zones in the Permian are spatially related to zones of intense basement cataclasis.

These strain data are included in Table 2 and on the maps and cross-sections of Figs. 9–20 in this present study. For clarity the data are coded as follows: G1D to

G3D—Daluis Gorges data (Graham 1978b, fig. 4); G1C and G2C—Cians Gorges data (Graham 1978b, fig. 5); G1T to G8T—Tinée valley and adjacent outcrops (Graham 1978b, figs. 6–10); G1V to G7V—Vionène valley data (Graham 1978b, fig. 11); G2R to G4R—Roya valley data (Graham 1978b, fig. 12).

Siddans (1980) used similar methods and obtained similar results from the south Daluis Gorges and the Tinée valley. Problems were found in the interpretation of the data and two models were considered:

(1) progressive pure shear superposed orthogonally on a compactional strain, such that the finite extension parallel with the bedding–cleavage intersection is zero and

(2) tectonic deformation at constant volume superposed on compactional strains of 41%.

When applied to the observed total strains the first model leads to volume reductions of up to 30% during the tectonic deformation, the second model implies up to 28% stretching along the bedding–cleavage intersection. These data (Siddans 1980, table 1) are coded SD for the locality in the south Daluis Gorges, S1–S5 for localities in the Tinée valley.

Kligfield *et al.* (1981a) provided further finite strain data and measured the anisotropy of magnetic susceptibility in rocks of known finite strain. The finite strain data were calculated from measurements of elliptical spot shapes on all available naturally occurring sections, using programs described by Owens (in press). Quantitative relationships were found between observed strains and magnetic susceptibility anisotropy, given by a linear relationship of the form $\epsilon_i = aM_i + b$, where ϵ_i are the observed principal logarithmic strains and M_i are the normalized differences between the principal susceptibilities and their geometric mean (Kligfield *et al.* 1981a, fig. 6). For the Alpes Maritimes redbeds the constants a and b are 25.65 and −0.0045, respectively (Kligfield *et al.* 1983). The observed finite strains (Kligfield *et al.* 1981a, figs. 3 and 4) again confirmed the pattern described by Graham (1978b). The data is here coded K1 to K20 and KA to KF, corresponding to sites 1–20 and A–F (Kligfield *et al.* 1981a, fig. 1, see also p. 184).

New data—analytic methods

Finite strain estimates have been made from analysis of green spot shapes at a further 18 sites: site number 17 in the Cians Gorges (Figs. 9–11), 1–4, 7–9 and 13 in the Tinée and Vionène valleys (Figs. 12–17), 14–16 and 18–23 in the Roya valley (Figs. 18–20). Site 8 is subdivided into four sectors, A, B, C and D, around an anticline (Fig. 16). In the absence of sufficient green spots, finite strains have been estimated from the quantitative correlation with anisotropy of magnetic susceptibility at sites 5 and 10–12 in the Tinée valley and at 49 points around the fold at site 8. Deformed or undeformed mudcracks are locally abundant and have been used to provide additional two-dimensional strain data in bedding planes and as an independent check on the strain estimates based on green spot measurement.

Finite strain analysis using green spot shapes. The strain analysis method used here is similar to that used by

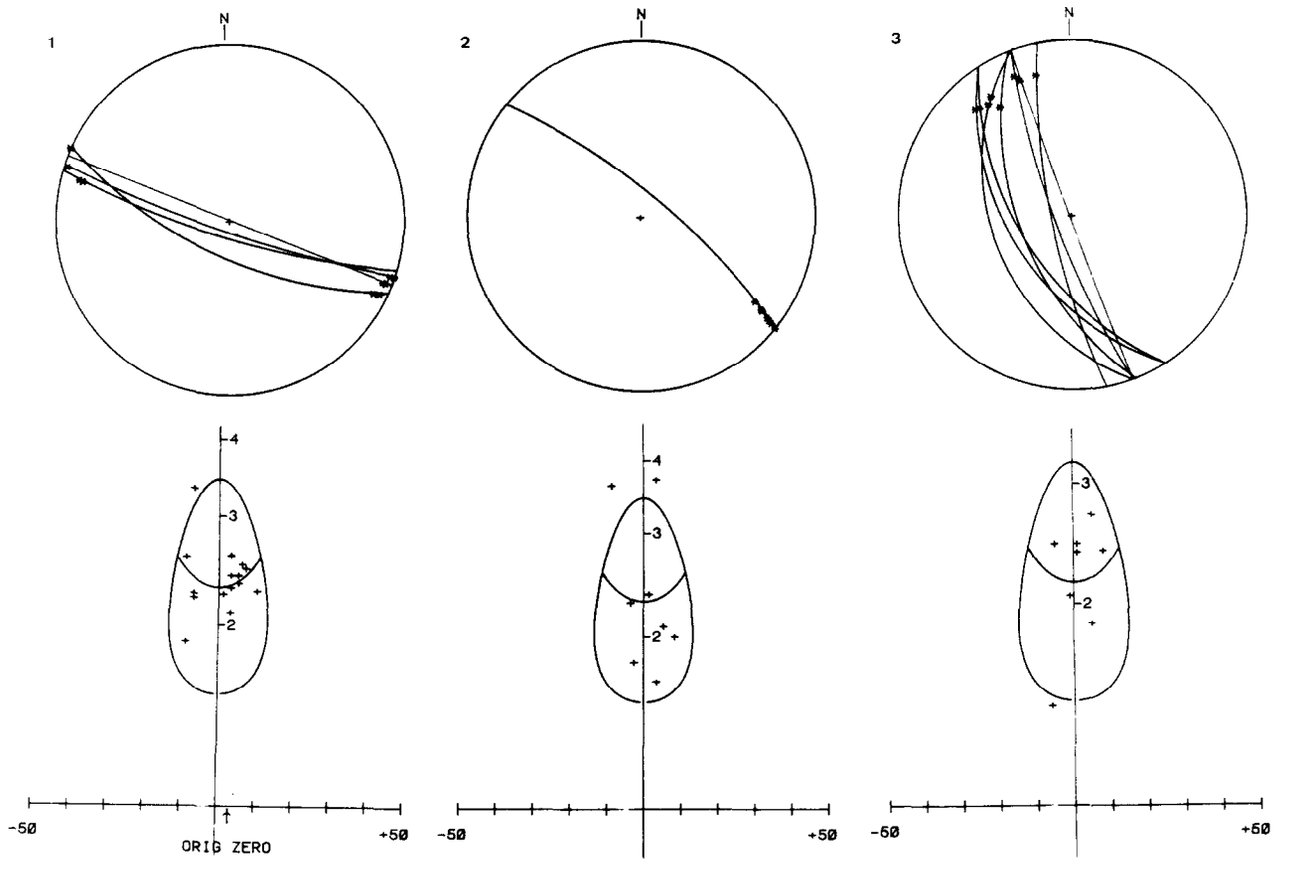

Fig. 4. (1–3).

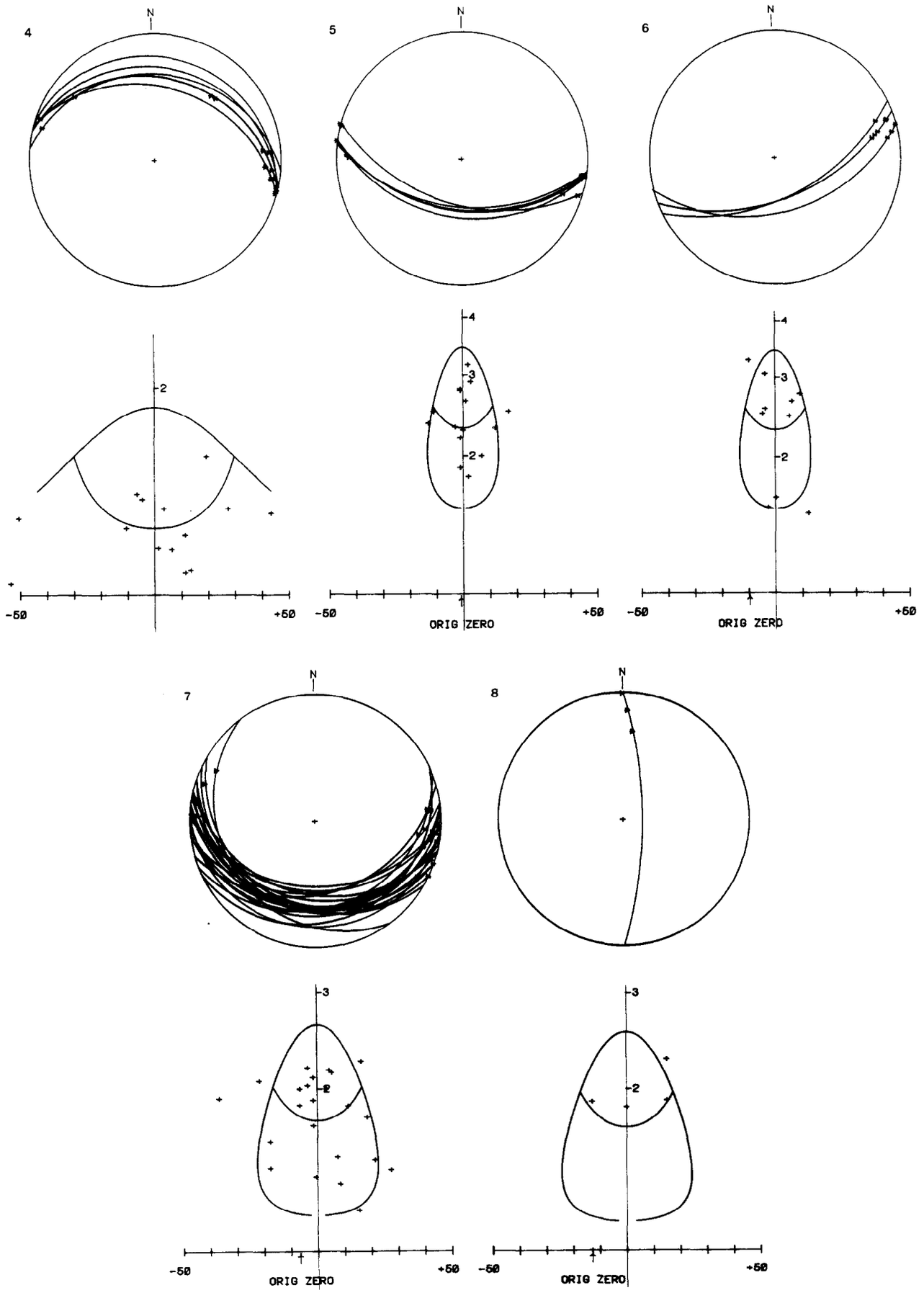

Fig. 4. Two-dimensional strain data for the mean section planes (1 to 8) used in the finite strain analysis at site 18. Upper: lower-hemisphere equal-angle projections of individual planes, crosses indicate long axis pitches. Lower: Rf/ϕ data for the mean planes. Corresponding numerical data is given in Table 1.

Kligfield *et al.* (1981a & b), based upon measurements of elliptical spot shapes (up to 218) on all naturally occurring sections at each site. In this study we have tried to improve the quality of the two-dimensional input to the first of the two programs written and described by Owens (in press), by grouping spot shape data from similarly oriented sections and estimating the finite strain ellipses on up to 15 differently oriented mean sections. The complete method is outlined below, using the analysis at site 18 as an example. The successive stages are:

(1) Measurement in the field, or on field oriented and scaled photographs, of naturally occurring sections (strike, dip) and the elliptical spot shapes on them (pitch of long axis, long axis, short axis). For site 18 the shapes of 101 spots on 47 sections were measured.

(2) Program DPEL9W, written in BASIC for the TEKTRONIX 4054A installation at Strasbourg, conversationally does all the two-dimensional data preparation and strain analysis for input to Owens' programs: The field data are entered sequentially and displayed stereographically, then grouped into similarly oriented sections, 1–8 for the site 18 data (Fig. 4) and the mean section orientations are calculated (Table 1). The 8 mean sections for site 18 include 99 of the 101 field measurements. When there are sufficient spots on a mean section the Rf/ϕ data is displayed and the best-fitting Rf/ϕ curves (Dunnet 1969) are established visually. When there is insufficient data on a mean section the strain ellipse is calculated using the method of Shimamoto & Ikeda (1976) and this estimate is used in the Rf/ϕ display. The 'original zero' marks on the ϕ-axes (Fig. 4) refer to strike directions in the mean sections. The strain ratio estimates for site 18, along with their long axis pitches, are given in Table 1. The mean sections are displayed stereographically with the pitches of their strain ellipse long axes (Fig. 5), enabling incoherent two-dimensional data to be identified. The mean section strain data is weighted according to its estimated reliability (Table 1), which is a function of the amount of raw data on the mean section and the quality of the Rf/ϕ diagram.

(3) The first-try ellipsoid program (Owens in press) provides up to six estimates of the finite strain ellipsoid, the best-fit ellipsoid program (Owens in press) provides a least-squares best-fit finite strain ellipsoid, normalized here to constant volume. Both programs calculate strain ellipse ratios and long axis pitches and the undeformed ellipse ratios in the input section planes, according to the calculated strain ellipsoid, together with a parameter r = logmean of the undeformed ellipse ratios (=1 for a perfect solution). The best-fit finite strain ellipsoid for site 18 has an associated r = 1.128 and the calculated data for the input section planes is given in Table 1.

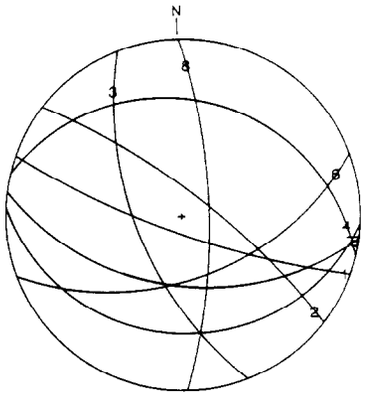

Fig. 5. Lower-hemisphere equal-angle projection of the mean section planes (1–8) used in the finite strain analysis at site 18. Numbers identify the planes and show the pitch of the strain ellipse long axes. See Table 1 for numeric data.

(4) Program EL9WDP provides graphic data presentation of the calculated ellipsoids. A Flinn diagram shows the shapes of the ellipsoids and a stereoplot their axial orientations referred to geographic coordinates, together with bedding and cleavage traces (Fig. 6). The spread of data points on these diagrams reflects the uncertainty of the calculated best-fit ellipsoid.

Two-dimensional finite strain analysis in bedding using deformed mudcracks. Deformed mudcracks are locally abundant in these rocks and enable independent estimates of the finite strain states in bedding planes to be determined. The strain state in the mudcrack layers was examined in the bedding plane at site 18 (Fig. 7). Two methods used to determine the strain state are described below.

The initial centres of undeformed mudcracks are commonly distributed in such a way that the distances between them are more or less constant. During deformation this non-random spatial distribution is modified

Table 1. Data for the eight mean section planes used in the finite strain analysis at site 18. Input data: strike and dip give the mean plane orientations, A and B are the semi-axes of the strain ellipses normalized to constant area, pitch is the long axis pitch, WT is a weighting factor; Calculated data: pitch and A/B are the corresponding values resulting on the same input planes in the calculated strain ellipsoid, a/b is the ellipse ratio resulting from the removal of the calculated strain from the input value.

ALPES MARITIMES '81 LOCALITY 18

	INPUT DATA							CALCULATED DATA		
N	STRIKE	DIP	PITCH	A	B	WT	A/B	PITCH	A/B	a/b
1	111	78	2	1,52	0,66	1,0	2,30	1	2,30	1,03
2	308	75	173	1,52	0,66	0,3	2,30	178	1,90	1,28
3	160	60	160	1,47	0,68	0,3	2,15	169	1,64	1,42
4	285	24	167	1,12	0,89	0,8	1,25	167	1,58	1,25
5	98	46	2	1,52	0,66	1,0	2,30	3	2,17	1,07
6	71	50	11	1,52	0,66	0,7	2,30	12	2,13	1,10
7	94	22	8	1,32	0,76	0,7	1,75	4	1,80	1,08
8	360	73	14	1,30	0,77	0,5	1,70	11	1,52	1,12

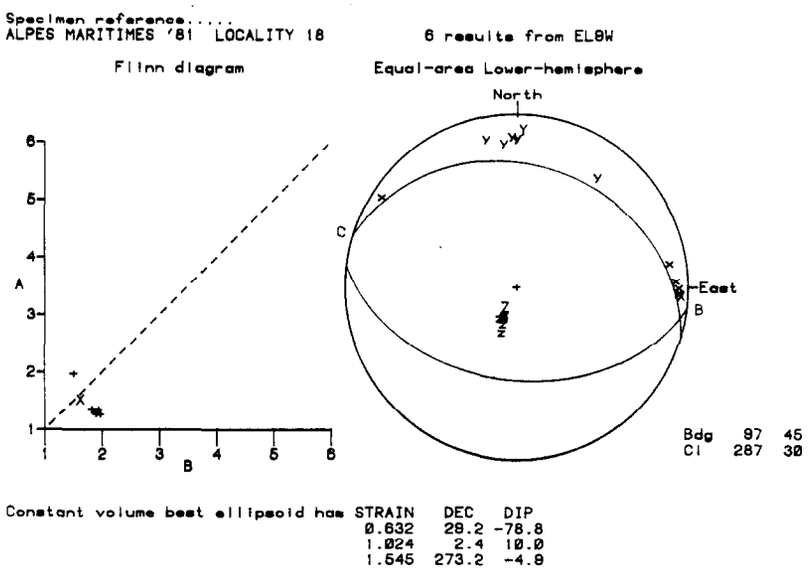

Fig. 6. Results of the finite strain analysis at site 18. Six small crosses on the Flinn diagram show individual ellipsoid estimates, the large X shows the best-fit ellipsoid. Axial orientations are similarly coded in the stereoplot.

by strain, with greater separation of mudcrack centres parallel to the long axis of the strain ellipse and least separation in the direction of the minimum strain axis. The 'all-object separation method' of Fry (1979) offers the possibility of using the above observations to determine the strain in the mudcrack layers. In the undeformed state, mudcrack centres can be determined using the intersections of chords joining the mid-points of mudcrack sides. After a homogeneous deformation the angular relationships between chords and sides are modified by strain, but the centres are still located by the intersection of the chords. The centres of 52 mudcracks were located using the above approach and used to determine the strain ellipse, using a digitized version of the graphic 'all-object separation method' (Hanna & Fry 1979) for the Tektronix system. The results (Fig. 8a) show a low point concentration around the central reference point, whose elliptical form specifies the shape ($Rs = 2.25$) and orientation of the strain ellipse.

If measures of shear strain (γ) can be made along two or more different directions, it is possible to calculate both the orientation (ϕ') and the ellipticity (R) of the strain ellipse. Lines were constructed from the centres of mudcracks to the mid-points of their sides and the deflection of these lines from a right-angle defines the angular shear (ψ), which is here taken to be positive for dextral shear and negative for sinistral shear. Figure 8(b) shows a plot of shear strain values determined from mudcrack sides having different orientations with respect to the site reference direction. The shear strain ($\gamma = \tan \psi$) and the orientation of the principal strain axes (ϕ') can be related to the strain ratio (R) by the expression

$$\gamma = [(R^2 - 1) \tan \phi']/(1 + R^2 \tan^2 \phi')$$

(Ramsay & Huber in press). When values of γ can be determined for different directions, then graphs can be constructed which can be used to evaluate the ellipticity (R) of the strain ellipse. These are the so-called 'Breddin Graphs' (Ramsay 1967, pp. 230–246, Breddin 1956). 39 values of γ and ϕ' were determined from measurements of mudcrack angular relationships and are shown in Fig. 8(b), upon which the Breddin Graph for a strain ratio of $R = 2.20$ is superposed. The two directions where the angular shear is zero are parallel with the two principal strain directions and the directions of maximum shear strain are found at approximately 26° to the axis of greatest extension. Although scattered the data do not deviate strongly from the Breddin Graph.

The strain ratio in bedding at this site 18 has been determined by three different methods:

(1) The 'all-object separation method' (Rs = 2.25)

(2) The Breddin Graph technique (Rs = 2.20)

(3) Rf/ϕ analysis of spot shapes (Rs = 2.29).

The 'all-object separation method' records the whole rock strain, as it is sensitive only to particle point positions in the rock during deformation. The Breddin Graph method records a strain ellipse which is dependent on the angular changes of mudcrack sides during deformation, a feature which is also distributed throughout the rock surface. The lack of significant difference in Rs values obtained using the different methods indicates that within the accuracy of the methods involved, the strain recorded by the spots is the same as that recorded by the mudcracks. This suggests that the spot shapes measured by us in this analysis and in previous studies, record the whole rock strain and also demonstrates the lack of competence contrast between spots and matrix.

Estimation of finite strains from anisotropy of magnetic susceptibility. Previous workers have shown that under favourable circumstances finite strain magnitudes and orientations can be determined directly from magnetic fabric studies in deformed mudstones and shales (Rathore 1979, Kligfield *et al.* 1981a). The magnetic susceptibility tensor (K_{ij}) specifies the relationship between the applied magnetic field (H_j) and the resultant magnetization (J_i) by the expression $J_i = K_{ij}H_j$. Mag-

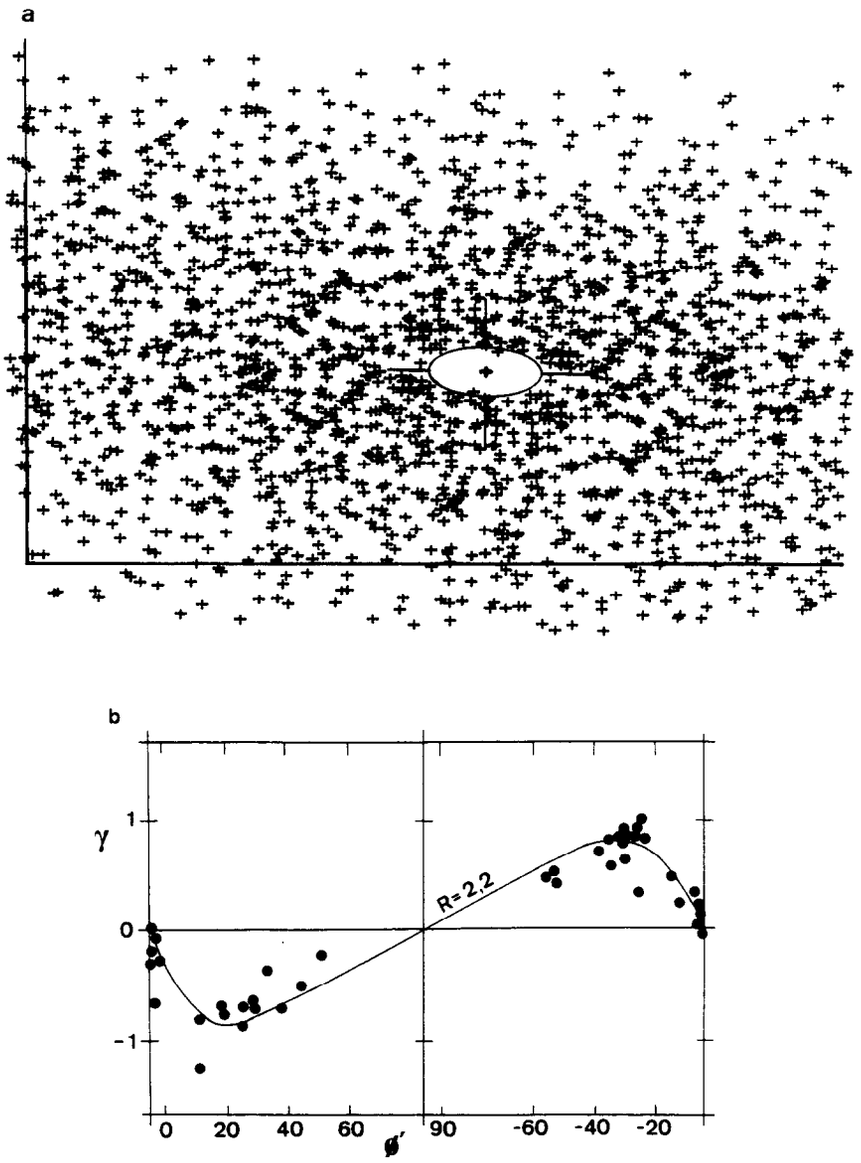

Fig. 8. Finite strain analysis in bedding at site 18 using the mudcracks shown in Fig. 7: (a) 'all-object separation' method using mudcrack centres; (b) γ v ϕ' data for mudcrack sides with the Breddin Graph for Rs = 2.20 superposed.

netic susceptibility is a second order tensor which can be represented geometrically as a triaxial ellipsoid, having principal axes $K_{max} > K_{int} > K_{min}$.

It has been demonstrated previously that hematite is the dominant magnetic mineral contributing to the magnetic fabric of the Alpes Maritimes Permian rocks and that the degree of magnetic anisotropy can be related to the preferred dimensional orientation of haematite particles in the rock (Henry 1973, van den Ende 1977, Kligfield *et al.* 1981a). As the latter is a function of strain it is apparent that the strain can be correlated with the amount of magnetic anisotropy in these rocks. Kligfield *et al.* (1981a) derived a quantitative expression between the magnetic anisotropy and the logarithmic strains in the Alpes Maritimes rocks. This relationship has been investigated in more detail by Kligfield *et al.* 1983). The data base was much enlarged by sampling a large number of additional sites encompassing a broad range of deformation states, including sites which showed only compactional deformation. Data from the 18 new sites augmented the original 7 to give a total of 25 sites. The relationship between logarithmic strain (ϵ_i) and the magnetic susceptibility anisotropy parameter (M_i) is given by $\epsilon_i = 25.65M_i - 0.0045$ and the correlation coefficient is 0.905. The slope of this regression differs from the results published in Kligfield *et al.* (1981a) for two reasons: recent instrumental improvements have resulted from cross-calibration of different measurement methods in various laboratories (Hrouda & Stephenson in press), and the increased size of the complete data set obviates the separation of the original small collection into two subsets by geographic area.

REGIONAL STRAIN PATTERNS

The finite strain data from this study, together with that already published by Graham (1978b), Siddans

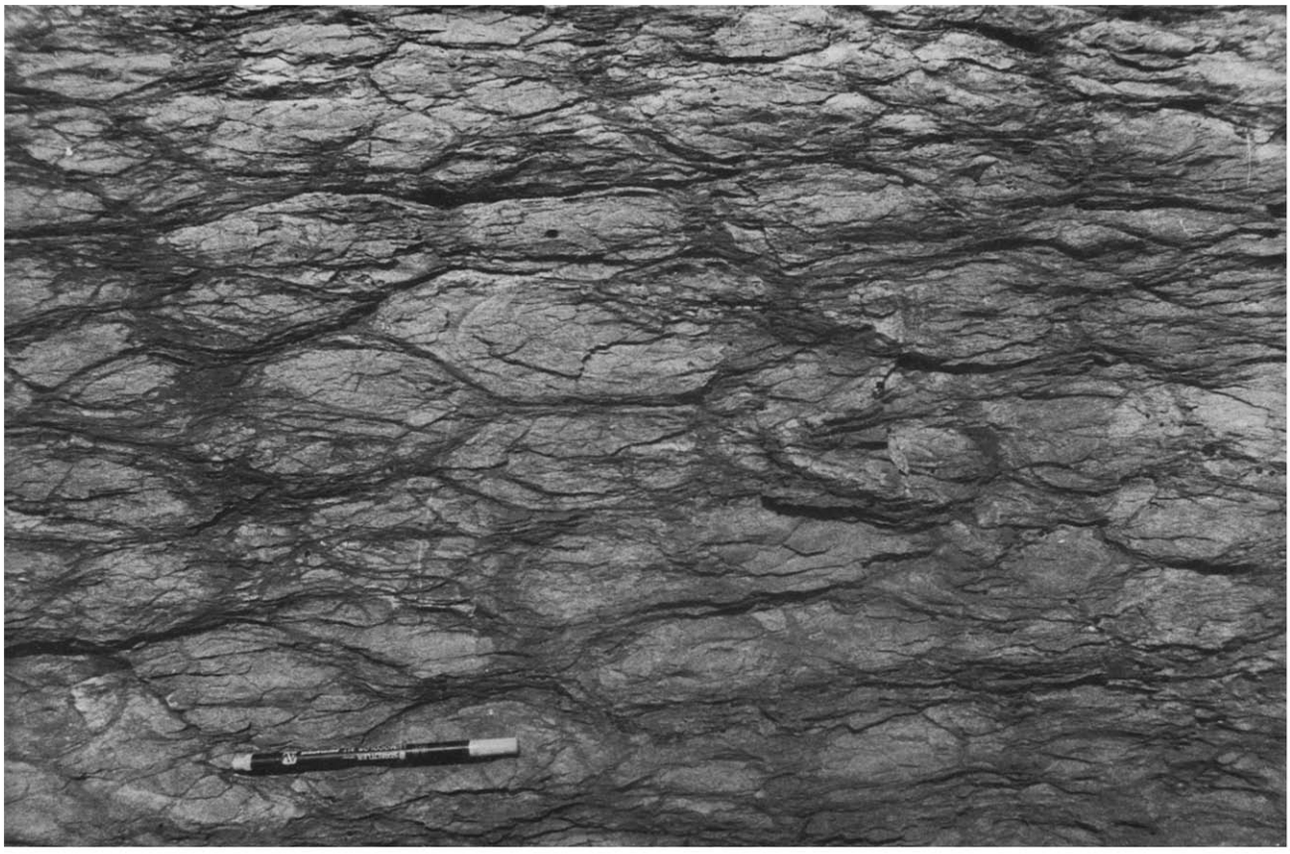

Fig. 7. Deformed mudcracks in bedding at site 18.

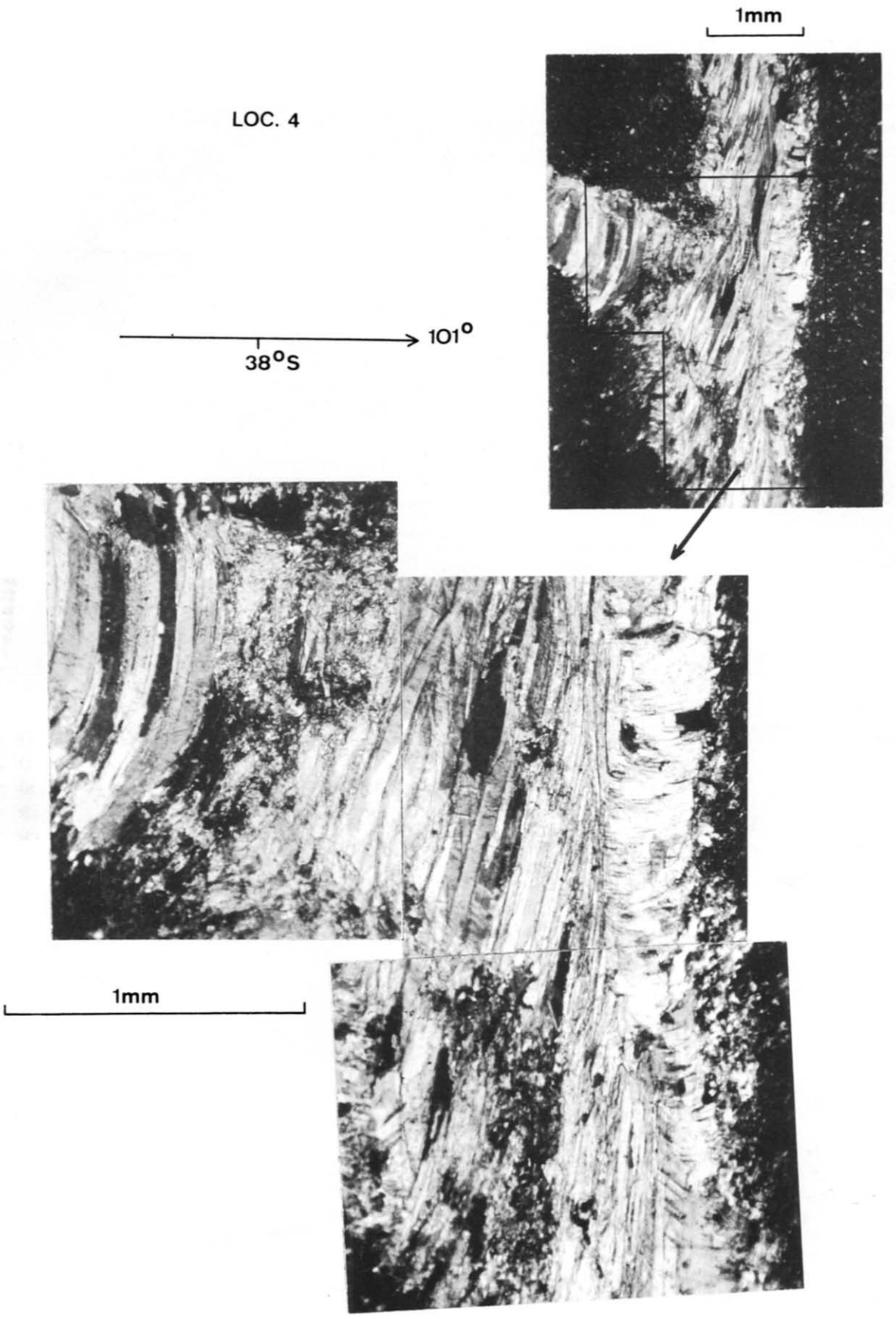

Fig. 24. Photomicrographs of syntaxial quartz fibres developed in cracks at site 4 in the Tinée valley. Corresponding orientation data are given in Fig. 25.

Table 2. Summary of published and new finite strain data from Permian rocks in the Alpes Maritimes. Coding and location of sites is explained in the text, the ellipsoid axial ratios are normalized to constant volume ($XYZ = 1$).

SITE	CONSTANT VOLUME ELLIPSOID			X		Z	
	X	Y	Z	AZ	PL	AZ	PL
G1D	1,19	1,19	0,70				
G2D	1,30	1,13	0,68				
G3D	1,21	1,01	0,81				
G1C	1,04	0,95	0,95				
G2C	1,40	0,87	0,82				
G1aT	1,46	0,92	0,74				
G1bT	1,51	0,81	0,81				
G2T	1,89	1,09	0,49				
G3T	1,36	1,36	0,54				
G4T	1,59	1,59	0,40				
G5T	2,36	1,41	0,30				
G6T	1,34	1,34	0,56				
G7T	1,46	1,08	0,64				
G8T	1,52	1,09	0,60				
G1V	2,24	1,19	0,37				
G2V	2,35	1,31	0,22				
G3V	1,90	1,45	0,36				
G4V	1,59	1,59	0,40				
G5V	1,84	1,47	0,37				
G6V	1,99	1,09	0,46				
G7V	2,05	1,03	0,47				
G8V	3,16	1,13	0,28				
G1R	1,53	0,96	0,68				
G2R	1,45	1,11	0,62				
G3R	1,57	1,42	0,46				
SD	1,19	1,19	0,70	110	0	020	80
S1	1,29	1,06	0,73	298	23	193	32
S2	1,33	1,02	0,73	099	9	356	54
S3	1,38	1,25	0,58	100	12	201	40
S4	1,47	1,34	0,51	115	33	190	25
S5	1,72	1,35	0,43	010	55	190	25
KA	1,19	1,19	0,70	282	15	094	75
KB	1,24	1,24	0,65	312	13	181	72
KC	1,46	0,92	0,74	097	17	247	70
KD	1,51	0,81	0,81	355	27	239	41
KE	1,57	1,42	0,45	302	12	200	45
KF	2,37	1,40	0,30	081	69	204	12
K1	1,17	1,08	0,79	256	1	164	58
K4a	1,38	0,95	0,76	319	4	057	8
K4b	1,35	1,04	0,71	316	26	220	11
K5	1,29	0,96	0,80	318	8	203	73
K6	1,29	0,90	0,87	302	13	203	33
K7	1,80	1,63	0,34	297	64	206	0
K8	1,44	0,86	0,81	105	6	197	23
K9	1,97	1,09	0,47	018	58	179	31
K11	1,55	1,25	0,52	102	24	203	33
K12	1,56	1,02	0,63	096	13	200	46
K13	1,42	1,20	0,59	096	25	187	2
K14	1,54	1,23	0,53	024	48	219	41
K15	1,39	0,95	0,76	091	8	344	64
K18	1,22	1,05	0,78	348	61	167	29
K19	2,81	1,02	0,35	041	79	198	10
K20	2,55	1,15	0,34	076	61	207	20
1	1,29	0,93	0,84	099	9	356	54
2	1,33	1,06	0,71	298	23	193	32
3	1,56	0,87	0,74	095	4	000	54
4	1,43	1,17	0,60	129	19	021	42
5	1,31	1,09	0,70	112	10	014	38
7	1,58	1,15	0,55	287	61	176	11
8A	1,66	1,36	0,44	351	47	229	26
8B	2,33	1,23	0,35	015	57	216	31
8C	2,94	1,01	0,34	017	53	210	36
8D	2,41	1,54	0,27	084	34	218	45
9	2,06	1,07	0,45	247	64	016	17
10	1,63	1,23	0,50	105	54	198	2
11	1,49	1,07	0,63	074	8	324	69
12	1,31	1,19	0,64	115	72	210	2
13	1,59	1,08	0,58	100	12	201	40
14	1,44	1,42	0,49	005	36	194	54
15	1,63	1,40	0,44	313	21	194	51
16	2,56	1,29	0,30	094	5	188	33
17	1,81	0,85	0,65	353	18	199	70
18	1,54	1,02	0,63	093	5	209	79
19	1,40	1,19	0,60	298	17	167	65
20	1,46	1,08	0,63	263	36	120	48
21	1,57	1,12	0,57	067	5	170	68
22	1,75	1,02	0,56	069	40	189	31
23	3.30	0,89	0,34	099	24	193	10

(1980) and Kligfield *et al.* (1981a), are summarized in Table 2. In the following maps and cross-sections, the finite strain ellipses that result on horizontal and vertical sections have been calculated from strain ellipsoids normalized to constant volume ($XYZ = 1$). Graham (1978b) did not precisely state the axial orientations of the finite strain ellipsoids that he determined, so these sites have been revisited and axial orientations determined. The nomenclature of stages (i)–(vi) in spot shape evolution, as identified by Graham (1978b) and summarized in the introductory remarks, has been retained in the following discussion to describe and compare spot shapes.

The Dôme de Barrot (Figs. 9–11)

Around the periphery of the Dôme de Barrot the Werfenian quartzites are either concordant with the Permian rocks, or overlie them with slight (2–3°) angular discordance. South to north traverses along the Daluis and Cians Gorges cross the western and eastern parts of the dome. In southern parts bedding dips up to 20°SSW in the Daluis Gorges and up to 55°S in the Cians Gorges. In northern parts the dips are up to 20°NNE or N. Cleavage in the Dôme de Barrot is generally non-existent in southern parts (sites K1, G1D, SD, KA). A cleavage trending 120–140° is weakly developed in northern parts of the Daluis Gorges and in central parts of the Cians Gorges (sites G2D, KB, G3D, K4, G2C). Its development in northern parts of the Cians Gorges is irregular, both geographically and in its intensity (sites K5, K6, G1C, 17; see Henry 1971, pp. 44–68, Graham 1978b, p. 224). Cleavage dips are generally 30° to 60°NE. Henry (1971, pp. 45–51) noted several peculiarities of the cleavage development, notably that just north of the Tête des Caires, in the eastern Dôme de Barrot, it is clearly superposed on a gently NE dipping thrust and a NW–SE trending, SW closing, recumbent fold in the hanging wall rocks.

The Daluis Gorges. In southern, southerly dipping parts, where there is no cleavage development, green spots are circular in bedding planes and flattened in the plane of the bedding (Siddans 1980, pl. 1a & b). Undeformed mudcracks and rain-pits in the bedding planes confirm this observation. Three independent estimates of the compaction (sites G1D, SD, KA) all suggest 41% shortening normal to bedding. The absence of any extensional features in the bedding planes suggests that this compaction was achieved by volume loss. These rocks represent the initial, stage (i), pre-tectonic deformation state.

In northern, northerly dipping parts, where there is weak cleavage development, spots are triaxial with X parallel to the bedding–cleavage intersection, 100° subhorizontal, and Z normal to bedding (sites G2D, G3D; cf. Siddans 1980, pl. 1c & d), or are oblate in bedding (site KB) with 48% compaction. These rocks represent stages (ii) and (i), respectively. Comparison of spot shapes at sites G2D and G3D shows that at lower

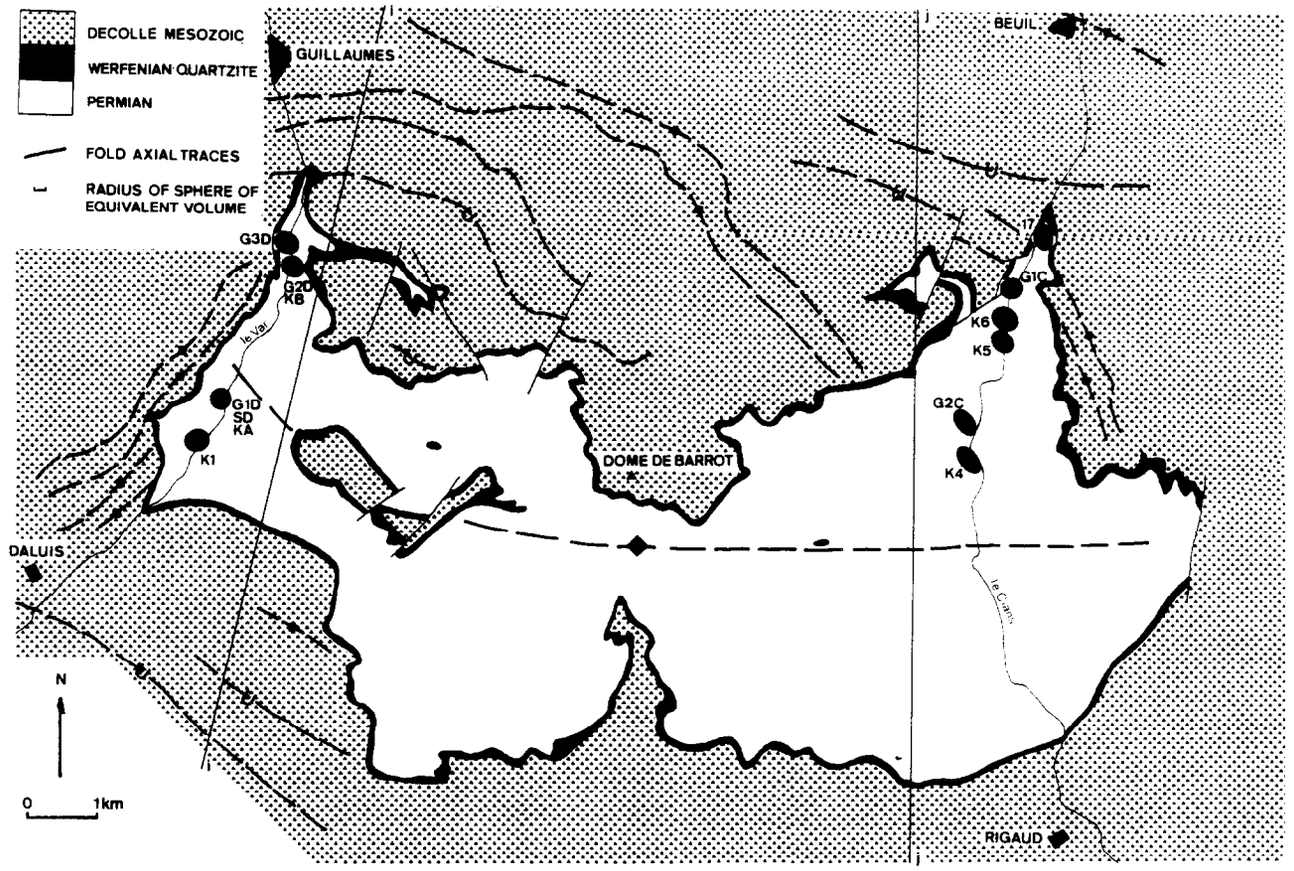

Fig. 9. Structural map of the Dôme de Barrot showing horizontal finite strain ellipses at numbered sampling sites.

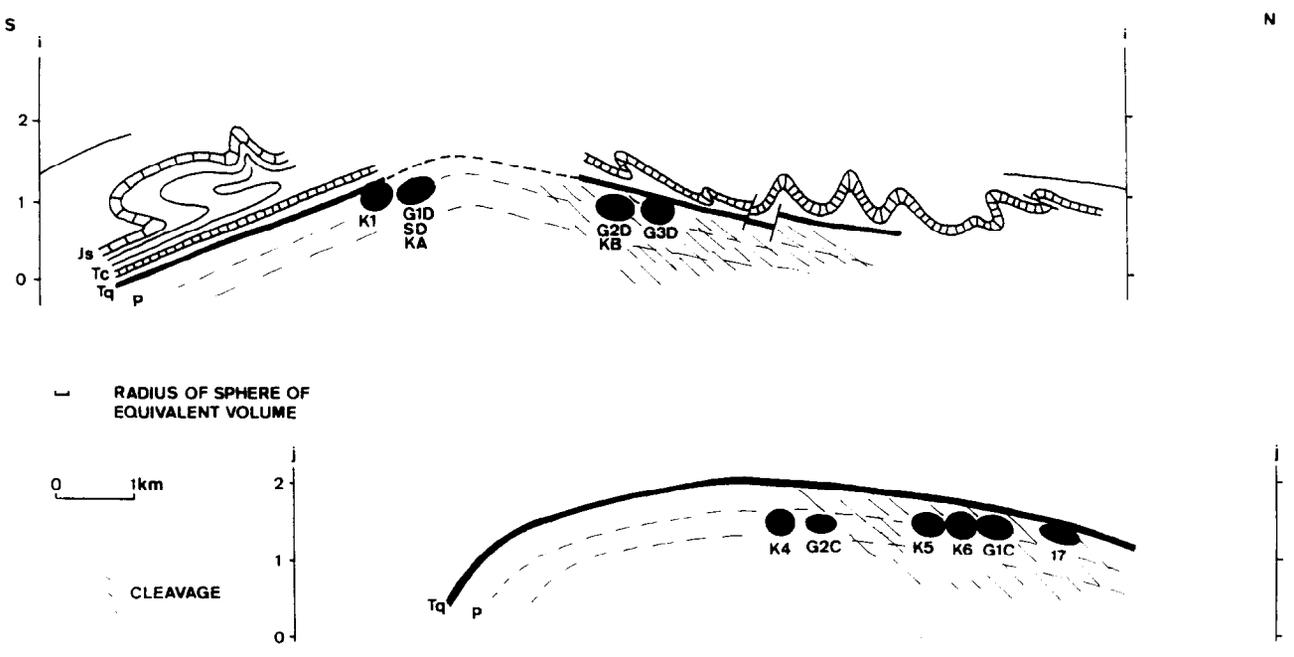

Fig. 10. Sections through the Dôme de Barrot showing vertical finite strain ellipses.

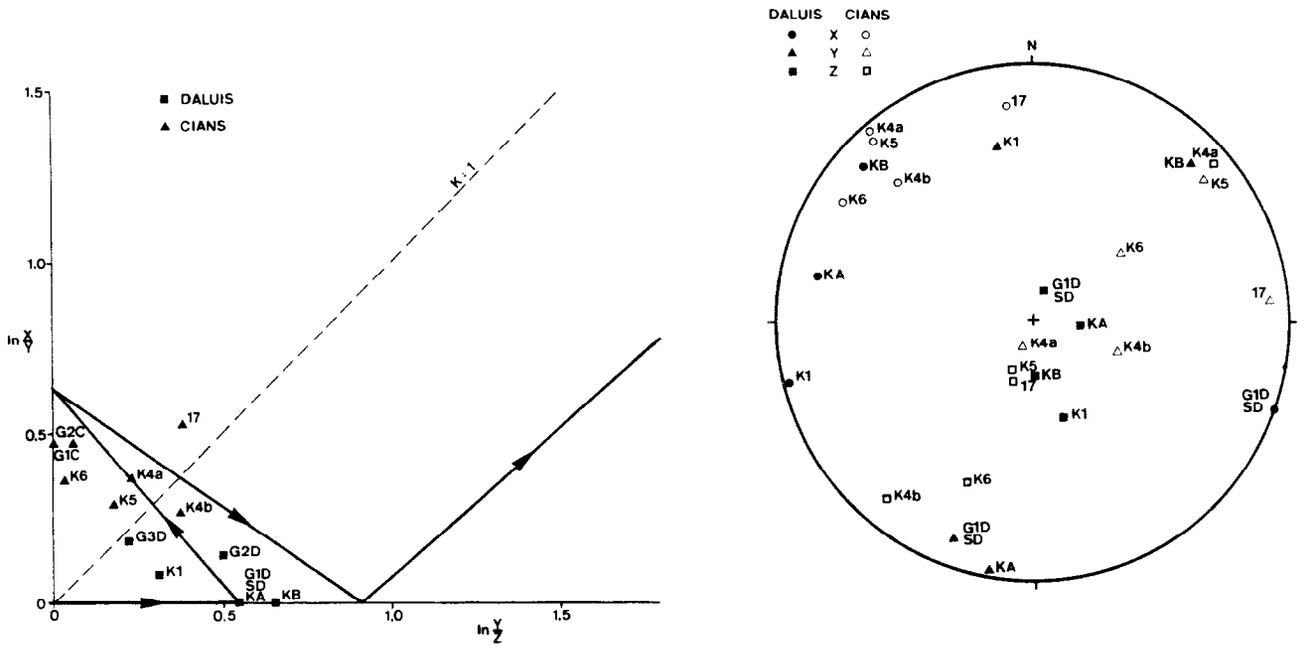

Fig. 11. Results of finite strain analyses in the Dôme de Barrot. Deformation plot is logarithmic, stereoplot is equal-area lower-hemisphere.

stratigraphic levels they plot in the flattening field of the Flinn diagram, $k < 1$, while at higher levels they lie almost on the line $k = 1$ (Fig. 11a). Note, however, the result from site KB, at about the same stratigraphic level as G2D, but with an oblate shape, $k = 0$.

The Cians Gorges. In northern parts of the Cians Gorges spot shapes are those of stages (ii), (iii) and (iv) (sites K5, G1C, 17). Stage (iv) shaped spots, with Z trending N 010–020° subhorizontal and Y subvertical, are found in the flat-lying central parts (sites G2C, K4). Graham (1978b, p. 224) notes that the Rf/ϕ data on YZ and ZX sections at site G2C show fluctuations towards bedding traces, i.e. the spot shapes are tectonically imbricate (cf. Dunnet & Siddans 1971, fig. 9).

The Tinée valley and Vionène valley regions

These outcrops are described as two sub-regions: the South Tinée (Fig. 12) and the North Tinée and Vionène (Fig. 13), following the geographic distribution of their different finite strain patterns. Graham (1978b, p. 221) notes the overstep of the Werfenian quartzites from Permian rocks in the southern and western parts, onto the crystalline basement to the north and east. This results from at least vertical tectonics during the pre-Triassic phase. Although little, if any, angular discordance is seen in the field in the South Tinée region, direct evidence of at least two deformation phases is frequently found in the Permian rocks:

(1) A pressure solution cleavage is often superposed on the slaty cleavage, e.g. at site KF just north of St. Sauveur. Normally the two cleavages have identical strike, but their dip relationships are inconsistent (see discussion in Graham 1978b, p. 222).

(2) The ESE trending, steeply NNE dipping slaty cleavage, e.g. at site 9, is folded by later open folds and crenulations plunging moderately ESE.

(3) Late, open, N–S trending flexures are superposed on the major ESE trending folds shown in Figs. 12, 13 and 14 (Bogdanoff 1980, p. 158, fig. 46).

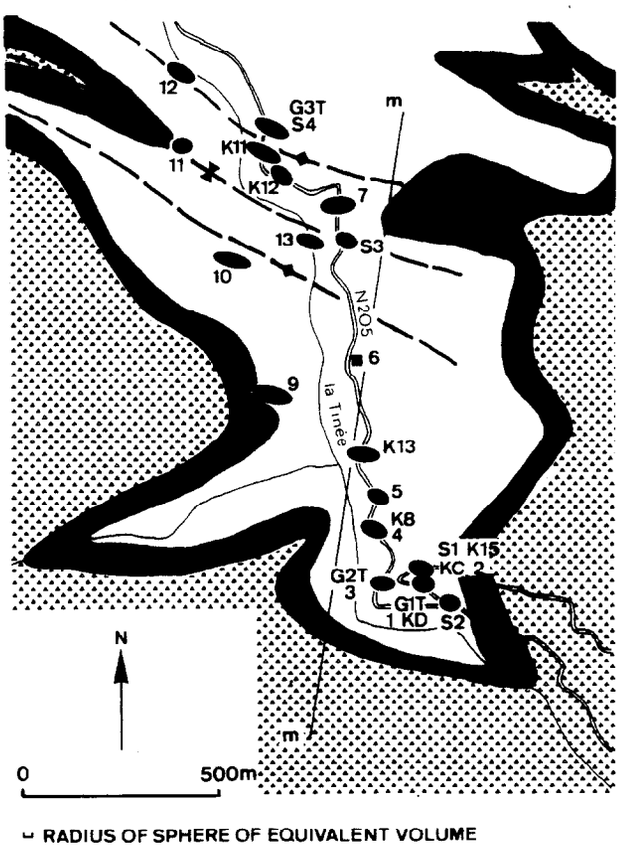

Fig. 12. Structural map of the South Tinée region showing horizontal finite strain ellipses at numbered sampling sites.

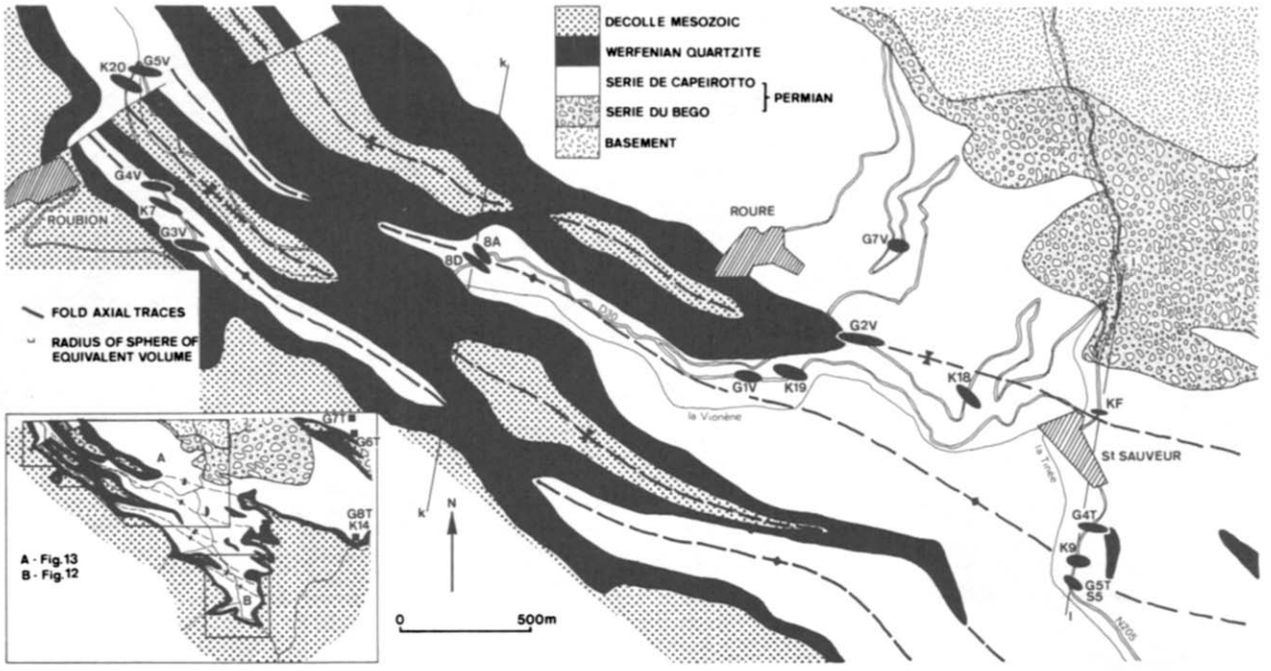

Fig. 13. Structural map of the North Tinée and Vionène region showing horizontal finite strain ellipses at numbered sampling sites.

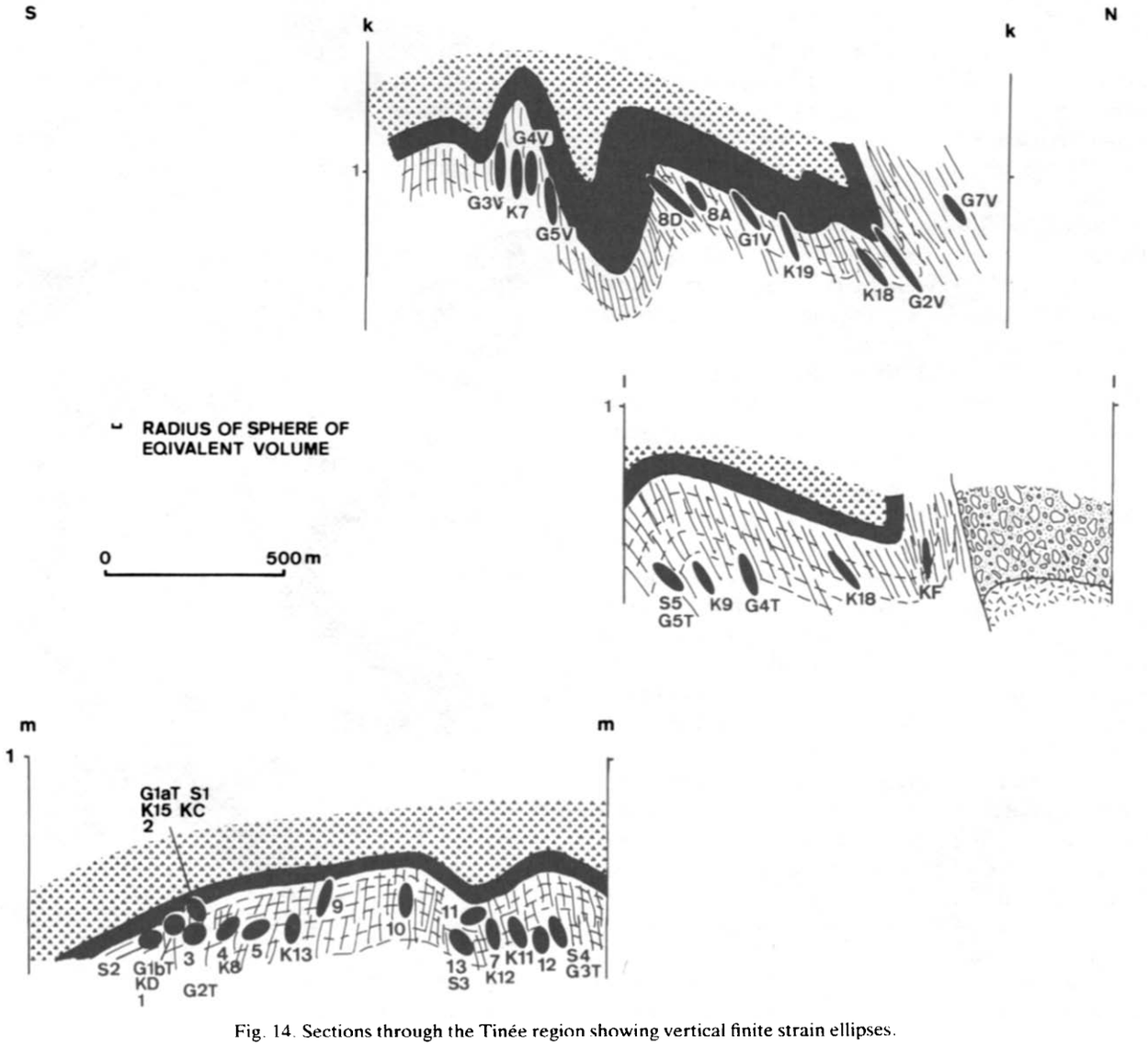

Fig. 14. Sections through the Tinée region showing vertical finite strain ellipses.

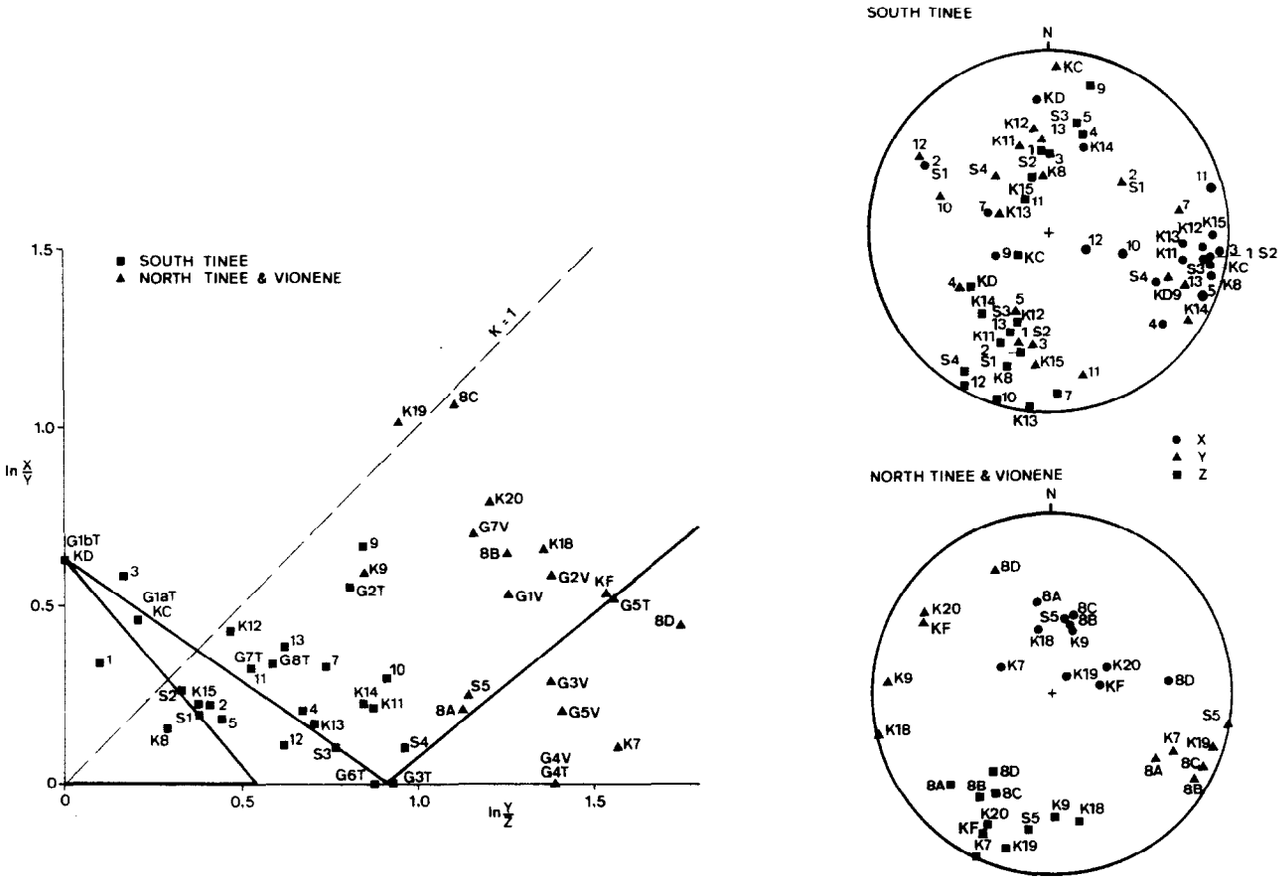

Fig. 15. Results of finite strain analyses in the Tinée region. Deformation plot is logarithmic, stereoplot is equal-area lower-hemisphere.

The ESE trending folds of both sub-regions (Figs. 12, 13 and 14) are upright in southern parts, but have axial surfaces and associated slaty cleavage inclined to the NNE in northern parts. The Série de Capeirotto outcrops are bounded to the NNE by reverse faults, which upthrow the stratigraphically lower Série du Bego and the basement. To the east of this Tinée region Permian rocks also outcrop near the Valdeblore refuse tip (sites G8T, K14) and in the Vallon de Cabane–Mt. Giraud region (sites G6T, G7T; see inset map in Fig. 13). These outcrops are described by Graham (1978b, pp. 228–230) as synclines above reverse faults in the basement and Série du Bego. The finite strain data from these sites links them naturally with the South Tinée region.

The South Tinée region (*Figs.* 12, 14mm, 15a & b). South to north along the SW dipping limb of the most southerly major fold in the South Tinée region, spots are variable from stage (ii) shapes in the extreme south (sites S2, 1), to stage (vi) shapes in the north (site 10). The variation, however, is not systematic, stage (ii) shapes are found as far north as site 5 (see sites K15, KC, G1aT, S1, 2, 3, 4, 5), while stage (iv) shapes make their most southerly appearance at site G2T and also occur at site K8. Stage (iii) shapes are found at sites G1bT and KD, geographically south of the first appearance of stage (iv) shapes. Spots with stage (iii) shapes are found in rocks that have pencil structure parallel with the bedding–cleavage intersection. Stage (vi) shapes, with X down-dip in the cleavage, occur at site 9. This site is just below the stratigraphic contact with the Werfenian quartzites. Apart from site 9 there is an increase in deformation state with increase in depth below the contact with the quartzites. Compare for example the stage (ii) spot shapes at sites 1, K15, KC, G1aT, S1 and 3, with the stage (iii) shapes at sites G1bT and KD, and the stage (iv) shapes at site G2T.

Further north in the South Tinée region, spots generally have stage (iv) shapes (sites 13, S3, K12, K11). The finite strain is still, however, variable. Site 11, just below the quartzites, shows stage (ii) shapes, cleavage is only poorly developed and pencil structure is the most striking feature of the rocks in outcrop. Stage (vi) shapes occur at sites 7 and 12, and oblate spots of stage (v), with Z normal to cleavage and circular sections in the cleavage surfaces, are found at site G3T.

The North Tinée and Vionène region (*Figs.* 13, 14k–k & 11, 15a & c). The finite strain pattern is here much more uniform. With the exceptions of sites G4T and G4V, which show oblate stage (v) spots, all sites have triaxial stage (vi) finite strain, with X more or less down-dip in the cleavage. X/Y ratios are generally higher on the steeply SW dipping or overturned limbs of folds, than on the NE dipping limbs. This ratio also increases when the steep (inverted) limbs from south-western parts are compared with those from the north-east, e.g. $X/Y = 1.56$ at site 8D, 1.99 at G7V and even 3.1 at G8V, in the section shown in Fig. 14k–k. Corres-

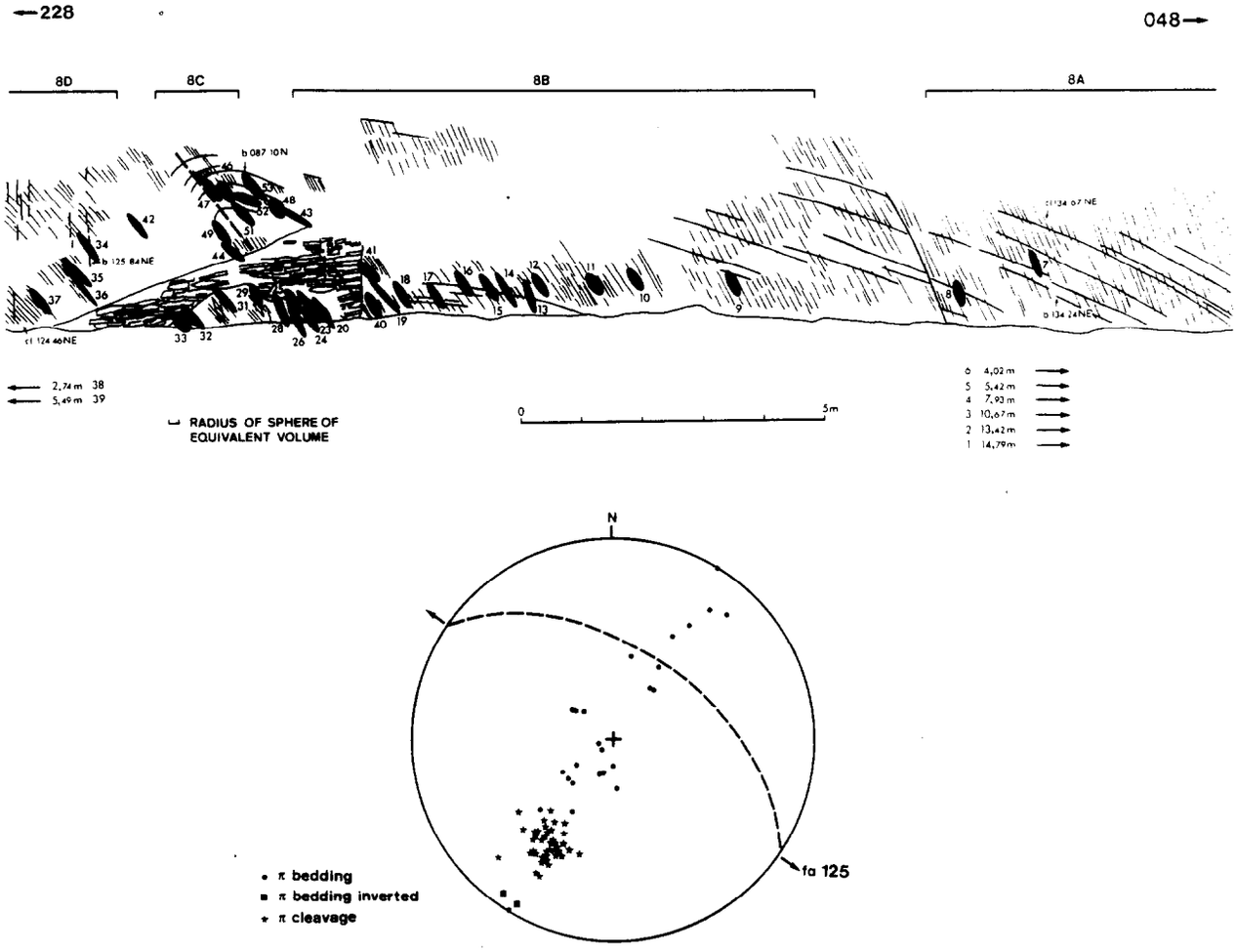

Fig. 16. Distribution of two-dimensional finite strain in a section through the anticline at site 8. Steroplot is equal-area lower-hemisphere.

ponding ratios for the same folds further southeast are rather lower, e.g. $X/Y = 1.27$ at site S5, and 1.69 at KF, in the section shown in Fig. 14l–l. Along the length of individual folds deformation seems to be higher in the Vionène valley than in the North Tinée valley.

The finite strain pattern around the anticline at site 8 has been studied in detail, using the quantitative correlation between observed finite strains and the anisotropy of magnetic susceptibility reported above for these rocks. The magnetic anisotropy is readily and quickly measured, and can then be promptly converted with the aid of this linear relationship into a strain value. This was done for each of the 49 samples from site 8, giving a rich collection of strain values. In the following discussion of the strain at site 8 the special origin of the indirectly obtained strain data should be recognized. The great circle of poles to bedding around the fold shows a fold axis with plunge 0° towards 125° (see inset stereoplot in Fig. 16). The steeply dipping SW limb is locally overturned, strongly developed slaty cleavage is approxi mately axial planar to the fold. The finite strain ellipses that are shown in Fig. 16 are those resulting in a profile section (035° vertical), through strain ellipsoids normalized to constant volume. It should be noted that the cross-section shown in Fig. 16 is not quite a profile section. The strain ellipses become more flattened in the cleavage from NE to SW across the fold, as cleavage dip decreases from 67°NE to 45°NE. The fold was divided into four sectors, 8A, B, C and D in the field (see Fig. 16) and finite strain estimates calculated on the basis of green spot measurements for each sector (see Table 2). These are indicated as the larger, unnumbered symbols in the logarithmic Flinn diagram and stereoplots of Fig. 17. Inspection of these diagrams shows that while the deformation fields for the four sectors overlap, the most highly deformed rocks are found in the hinge zone and the steep SW limb (sectors C and D). The stereoplots show that the axial orientations of the finite strain ellipsoids vary systematically across the fold.

Sector A: Z-axes cluster about the pole to cleavage (plunge 15° to 221°), X-axes have 0–65° NW pitches in the XY plane.

Sector B: Z-axes cluster about the pole to cleavage (plunge 35° to 216°). The pitches of X-axes are dispersed through all orientations in the XY plane.

Sector C: Z-axes cluster about the pole to cleavage (plunge 40° to 216°). X-axes have pitches dispersed through all orientations in the XY plane.

Sector D: Z-axes cluster about the pole to cleavage (plunge 42° to 210°). X-axes have pitches in the XY plane ranging from 50°NW to 30°SE.

These changes correspond with the decreasing dip of

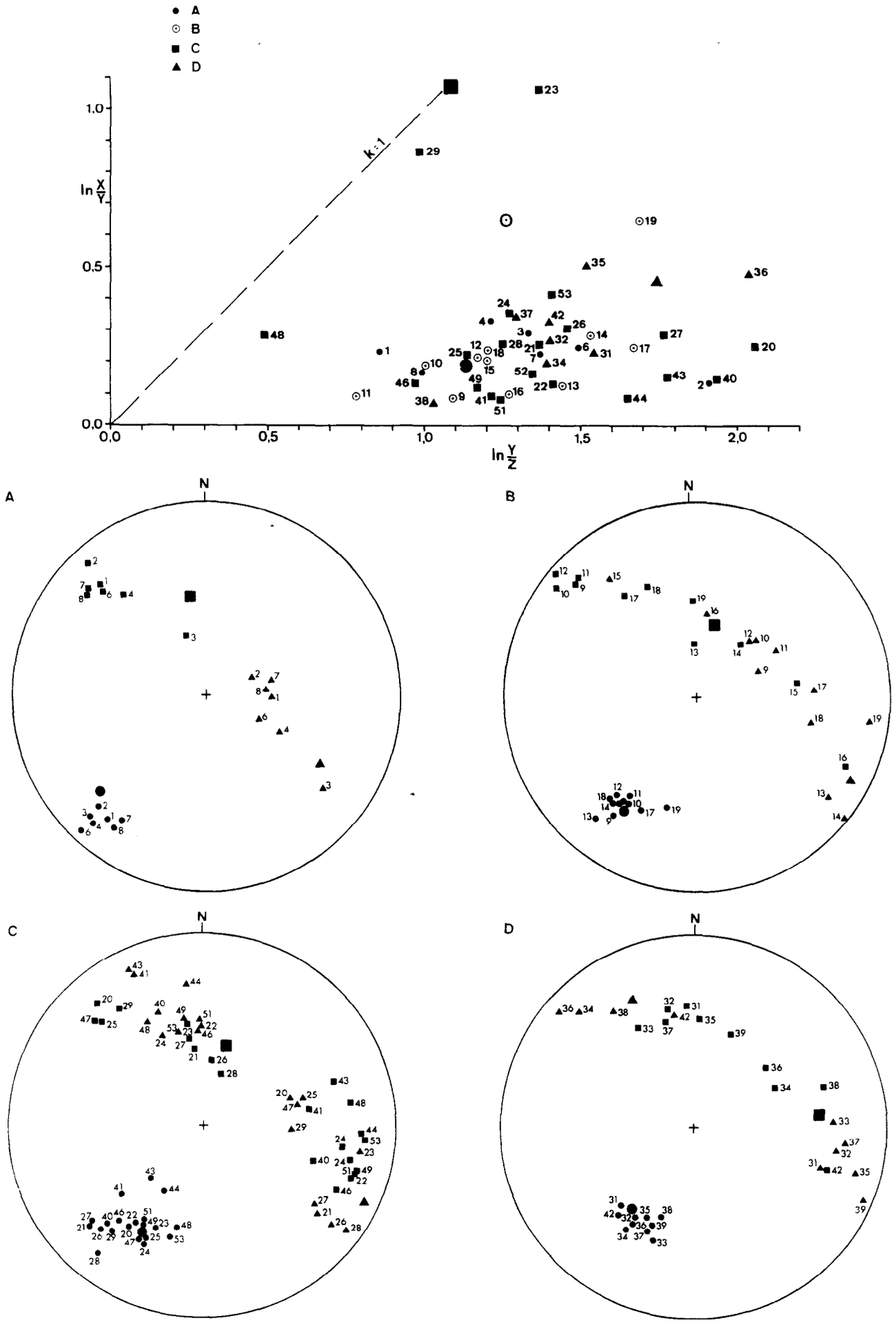

Fig. 17. Results of finite strain analyses around the anticline at site 8. Deformation plot is logarithmic, stereoplots are equal-area lower-hemisphere. A to D are the sectors shown in Fig. 16. Symbols on stereoplot are: squares, X; triangles, Y; circles, Z.

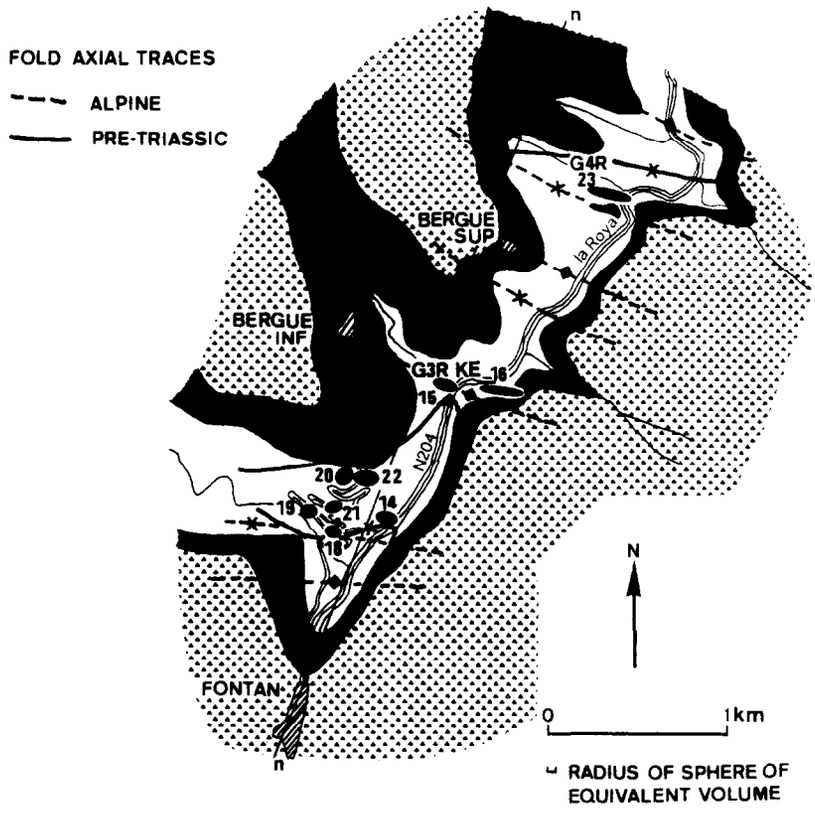

Fig. 18. Structural map of the Roya region showing horizontal finite strain ellipses at numbered sampling sites.

the cleavage across the fold and the pattern of finite extension seen generally in the Tinée and Vionène region, with increase in total deformation the finite extension direction becomes down-dip in the cleavage. Further interpretation of the finite strain pattern around this fold will be presented elsewhere.

The Roya valley region (Figs. 18–20)

The Roya valley region is notable for the clarity with which the pre-Triassic folds are seen, just north of Fontan (Figs. 18 and 19). Sites 14 and 18–22 are all from the steep southerly dipping, or even overturned limb of a pre-Triassic fold, with slaty cleavage dipping 20–45°N. Sites 15 and 16 are nearer the hinge of this anticline, where bedding dips about 30°S and cleavage about 50°N. Bedding at site 23 dips gently SE, the cleavage trends 120° and is almost vertical. To the north the Série de Capeirotto is fault-bounded against the Série du Bego.

Although variably oriented, following the geometry of the pre-Triassic folds, the distribution of the finite strain states is relatively uniform. Sites 14 and 15 show spot shapes that are just into the stage (vi) field, all other sites show stage (iv) spot shapes. The finite strain ellipsoid at site 23 has a logarithmic k-value of 1.37 and it plots all alone on the Flinn diagram (Fig. 20). At sites 20 and 21 the orientations of the principal extension direction and the principal magnetic susceptibility axis, although agreeing well with each other, are both rotated by about 50–60° anticlockwise from the regional attitudes. The remanent magnetization directions for these two sites are rotated by an equivalent amount

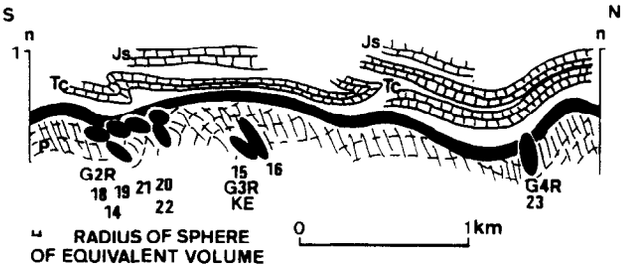

Fig. 19. Section through the Roya region showing vertical finite strain ellipses.

away from the stable Permian direction for the Alpes Maritimes region (Kligfield *et al.* 1983).

DISCUSSION

Geometric aspects of the finite strain pattern

In many ways the three axis planar diagram provides a more useful way of considering three-dimensional strain states than the Flinn diagram (Owens 1974). The strain data, normalized to constant volume, is plotted on such a diagram in Fig. 21. The choice of axes and nomenclature here is identical with that used by Kligfield *et al.* (1981a, fig. 4): r parallels the bedding–cleavage intersection; p is normal to cleavage; q lies in the cleavage perpendicular with the bedding–cleavage intersection. The axes are scaled in this figure (and in all the three axis diagrams that follow in the subsequent discussion), such

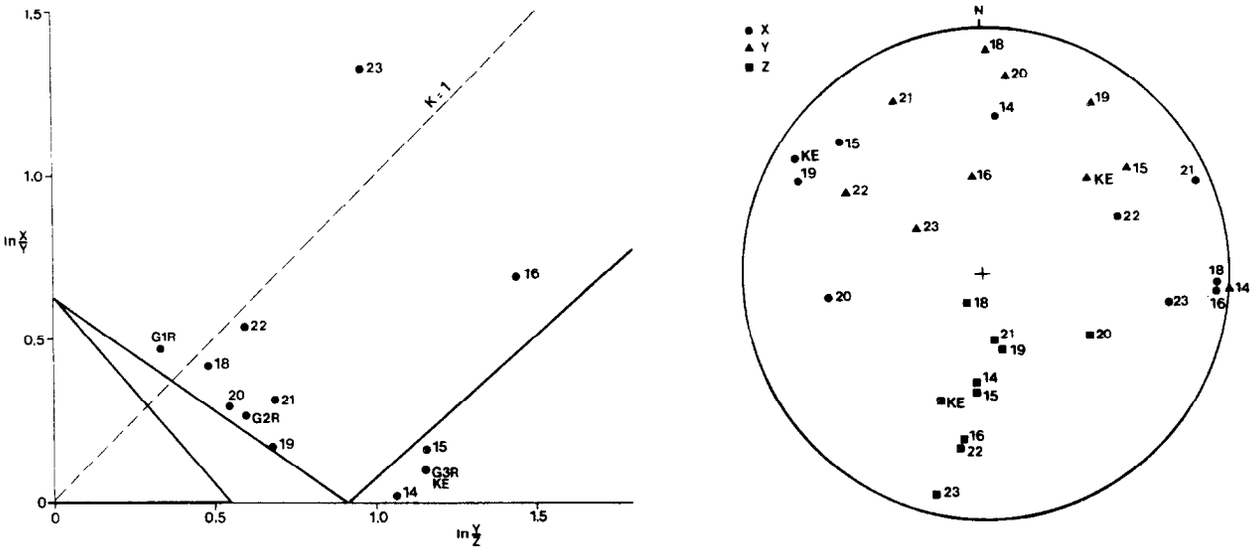

Fig. 20. Results of finite strain analyses in the Roya region. Deformation plot is logarithmic, stereoplot is equal-area lower-hemisphere.

that any point on the diagram represents an ellipsoid with volume $4\pi/3$. In this region of the Alpes Maritimes r is thus generally oriented 100–120° subhorizontal, p is generally 010–030° subhorizontal in southern parts of the Tinée region and with a SSW plunge elsewhere. The succession of finite strain stages (i)–(vi), resulting from progressive pure shear superposed orthogonally on diagenetic compaction, is also shown in Fig. 21. Compacted but tectonically undeformed rocks of stage (i) plot along $-q$, the prolate stage (iii) shapes plot along r and the oblate stage (v) state along $-p$. The finite strain states in Fig. 21 are coded according to the geographic sub-regions and ignoring some apparently anomalous results, the deformation fields associated with each sub-region have been outlined. The result of this exercise is a highly systematic arrangement of deformation fields.

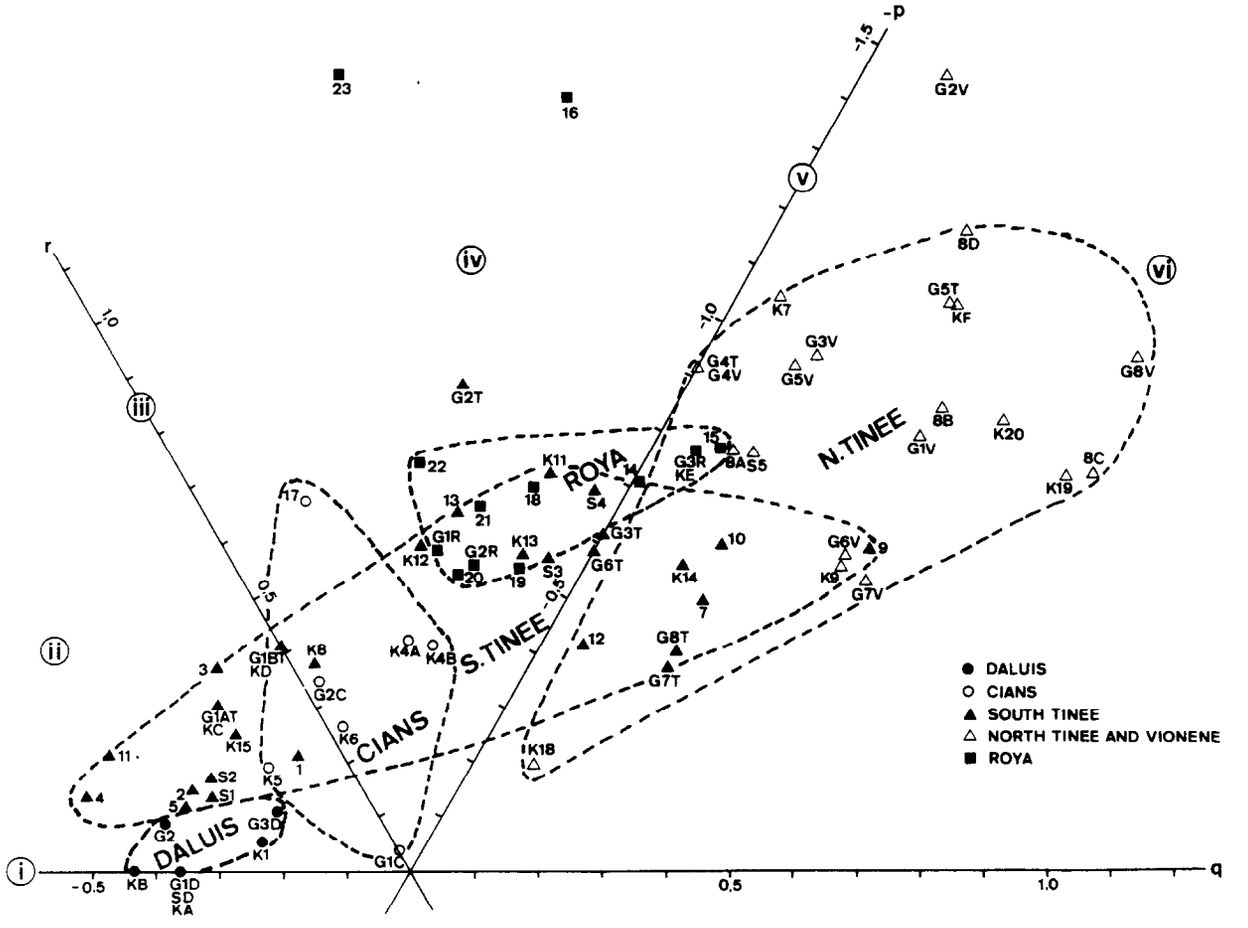

Fig. 21. Three axis planar diagram of finite strain analyses, showing the fields of finite deformation stages (i)–(vi) and the deformation fields for the geographic sub-regions. See Table 2 for corresponding numerical data.

The Dôme de Barrot rocks plot in the ranges of stages (i)–(iv), the Daluis Gorges rocks at stages (i) and (ii), the Cians Gorges rocks straddle the stage (iii) line. South Tinée rocks plot in a band extending from the stage (ii) to the stage (vi) fields, the North Tinée and the Vionène rocks continue the same band from the stage (v) line further into the stage (vi) field. Rocks from the Roya region overlap the South and North Tinée fields in their parts representing rocks with relatively high r values and mainly in the stages (iv)–(v).

Compaction and orthogonally superposed pure shear model. The idealized sequence of spot shapes (i)–(vi), as discussed by Graham (1978b) and outlined in the introductory remarks, results from diagenetic compaction by volume loss, followed by orthogonal superposition of tectonic pure shear, with tectonic shortening (Z_t) parallel to bedding, tectonic extension (X_t) normal to bedding and the intermediate tectonic strain axis ($Y_t = 1$) parallel to the bedding–cleavage intersection. The three axis diagram of finite strain states resulting from this particular model of deformation can have two sets of lines superposed on it (Fig. 22):

(1) Lines of equal compaction by volume loss (0, 10, 20 . . . 95%). These are lines normal to the r axis and make equal intercepts on the $-q$ and $-p$ axes.

(2) Lines of equal X_t/Z_t ratio (1, 5, 2, 3 . . . 100) for the tectonic pure shear ($Y_t = 1$) at constant volume, with elongation along q and contraction along p. These are lines parallel with the q axis and make equal intercepts on the r and $-p$ axes. Deformation paths resulting from compaction by volume loss are all along the $-q$ axis, e.g. O–KA and O–KB, representing 0–41% and 0–48% compaction, respectively. Deformation paths resulting from orthogonally superposed tectonic pure shear are perpendicular to the r axis and follow lines of equal compaction, e.g. KB–8B represents the effect of increasing the X_t/Z_t ratio of the pure shear ($Y_t = 1$) from 1 to 14, after initial compaction of 48%. The resulting ellipsoid, at point 8B, has normalized axial ratios of 2.33 : 1.23 : 0.35. The deformation fields of Fig. 21 have been reproduced on the three axis diagram of Fig. 22. It is seen that all the deformation fields for the geographic sub-regions lie in a band between the 0% and 80% compaction lines, extending from X_t/Z_t ratios for pure shear of 1 to 40. The effect of incremental volume loss during the tectonic pure shear is to increase the slope of the deformation path, e.g. line KA–KF represents progressive pure shear from $X_t/Z_t = 1$ to 27, with incremental volume loss at 0.03, after an initial compaction of 41%. This is the deformation path discussed by Graham (1978b, fig. 15) for the Permian rocks of the Alpes Maritimes.

Deformation histories of this sort: compaction by volume reduction followed by orthogonally superposed progressive pure shear at constant volume, with tectonic extension normal to bedding and contraction parallel to bedding, produce rocks with two characteristic features:

(1) Cleavage is perpendicular to bedding and both parallel principal planes of the finite strain ellipsoid.

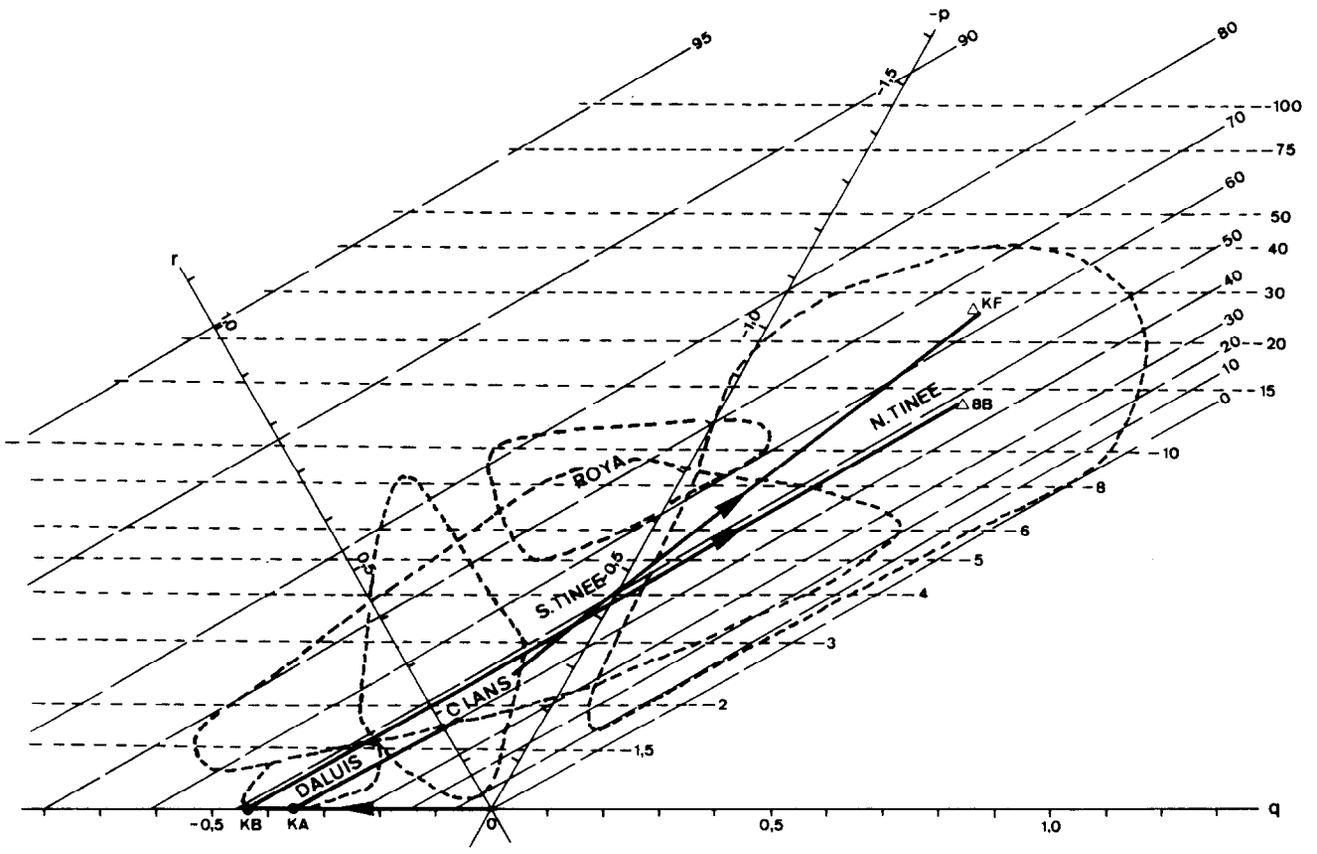

Fig. 22. Three axis planar diagram showing lines of equal compaction and equal pure shear ratio, according to the orthogonally superposed pure shear model (see text for details). Deformation fields for the geographical sub-regions and some deformation paths are also shown.

(2) There is no change in length along the bedding–cleavage intersection. While cleavage and bedding are approximately perpendicular in parts of the South Tinée section, elsewhere this is only locally the case in fold hinges. At site 8B for example, on the gently dipping northern limb of an anticline, bedding is oriented 314° with dip 24°NE, cleavage 304° with dip 59°NE. The finite Y direction is parallel with the bedding–cleavage intersection, with plunge 8° towards 119°. The plunge of the finite X direction is 1.8° less than the cleavage dip, which is the tectonically imbricate situation resulting from oblique superposition of pure shear on a pre-existing planar shape fabric (cf. Dunnet & Siddans 1971, fig. 9). The geometry of the total deformation is monoclinic in symmetry.

Compaction and obliquely superposed pure shear model. In order to investigate the effects of such oblique superposition, theoretical three axis diagrams have been computed for constant volume pure shear ($Y_t = 1$ parallel with the bedding–cleavage intersection), at different angles, ζ, between the tectonic shortening direction (Z_t) and the initial bedding orientation, together with tables of bedding trace behaviour in Z_tX_t section. Figure 23(a) shows such a diagram for $\zeta = 10°$. Comparison with Fig. 22 shows that while lines of equal compaction remain unchanged, the lines of equal X_t/Z_t ratio have a curved form and are discontinuous across the r axis. The extent of this discontinuous region about the r axis depends upon the angle ζ. It increases rapidly at first as ζ is increased from 0 to about 10°, then more slowly and it never includes the $-p$ axis. The implication of this discontinuous region is that for the case of constant volume oblique pure shear superposed on an initial compaction fabric, the perfectly prolate stage (iii) shapes, parallel with the bedding–cleavage intersection, do not occur. This arises from the different orientational significance of the axes in the case of obliquely superposed pure shear. r is still always parallel to the bedding–cleavage intersection and to one of the principal axes of the finite strain ellipsoid (X in the stages (ii) and (iv), Y in stage (vi)). p and q lie in the plane perpendicular to the bedding–cleavage intersection and still parallel to two of the finite strain ellipsoid axes: p is that nearer in orientation to the cleavage normal (Y in stage (ii), Z in stages (iv) to (vi)); q is that closer in orientation to the cleavage trace (Z in stage (ii), Y in stage (iv) and X in stage (vi)). Deformation paths representing the finite strain ellipsoid evolution according to this model, still follow equal compaction lines, but now jump over the discontinuous region about the r axis.

Consider in Fig. 23(a) the deformation path starting at point KB, representing a 48% compaction by volume loss prior to tectonic strain. The corresponding logarithmic Flinn diagram representation and a stereoplot of axial orientations are shown in Figs. 23(b) & (c). With increase in obliquely superposed tectonic pure shear ($Y_t = 1$, $\zeta = 10°$), the finite strain state moves along a deformation path normal to the r axis, as far as point H, at which it has $X:Y:Z = 1.24:0.95:0.85$ (parallel to $r:p:q$). The finite strain ellipsoid has a logarithmic k-value of 2.40 (Fig. 23b), and the long axis of the finite strain ellipse in section perpendicular to the bedding–cleavage intersection is oriented at 45° to the tectonic extension direction (X_t) (Fig. 23c). The X_t/Z_t ratio of the tectonic pure shear producing this finite strain state is 1.82, represented by the point H' in Figs. 23(a) & (b). This finite strain state is as close as it ever gets to the perfectly prolate stage (iii) shape, for at this stage in the progressive deformation the p and q axes swop over their correspondence with Y and Z (Fig. 23c), the deformation path on the three axis diagram jumps to point H^* in the stage (iv) field (Fig. 23a), with $X:Y:Z = 1.24:0.95:0.85$ (parallel to $r:q:p$). There is no discontinuity in the logarithmic Flinn diagram representation of the deformation path (Fig. 23b), in which the corresponding points H and H^* are identical and progress along the deformation is simply reversed.

With further increase in the X_t/Z_t ratio of the tectonic pure shear to 3.30 (represented by point L' in Figs. 23a & b), the current finite strain ellipsoid has axial ratios $X:Y:Z = 1.24:1.24:0.65$ (parallel to $r:q:p$), represented by point L in Fig. 23. It has the perfectly oblate stage (v) shape, the r and q axes swop over their correspondence with X and Y and the deformation path enters the stage (vi) field at $X:Y:Z = 1.24:1.24:0.65$ (parallel to $q:r:p$). Note that for constant volume tectonic pure shear, points L and KB are coincident on the logarithmic Flinn diagram representation of the deformation path (Fig. 23b). In this particular case the oblate stage (v) state is attained when the XY plane of the finite strain ellipsoid is inclined at 12° to the cleavage (Fig. 23c). Continuing along the same deformation path, in the stage (vi) field, the point 8B is attained when the X_t/Z_t ratio of the pure shear is 12. In this particular model the bedding in its post-compaction, pre-tectonic state was inclined at 80° to the future cleavage plane (X_tY_t) and its final orientation after oblique pure shear ($\zeta = 10°$, $X_t/Z_t = 12$, $Y_t = 1$) is at 25.3° to the cleavage. These orientations are represented by the great-circles α and α', respectively in Fig. 23(c).

Of the 78 finite strain analyses listed in Table 2, sites KA, KB, G1D and SD exhibit compaction and no measurable superposed tectonic strain. Only site G1bT, in the South Tinée region, has bedding and cleavage exactly perpendicular and a finite strain state that is exactly prolate (stage (iii)) parallel with the bedding–cleavage intersection. Following the principles of Fig. 22, this site can thus be interpreted in terms of an initial 70% diagenetic compaction by volume loss, then orthogonal superposition of a tectonic pure shear with axial ratios $X_t:Y_t:Z_t = 1.87:1.00:0.53$, where the tectonic shortening direction is about 010° horizontal and the tectonic extension is about vertical (see Graham 1978b, p. 226). At all other sites where the spots have near prolate shapes and where bedding and cleavage orientations are known (G1C, G2C), bedding and cleavage are not perpendicular and elliptical sections through spots show fluctuation towards the bedding trace (see Graham 1978b, p. 224). Sites 1, 3, 8B, 13, 17 and 18 all have

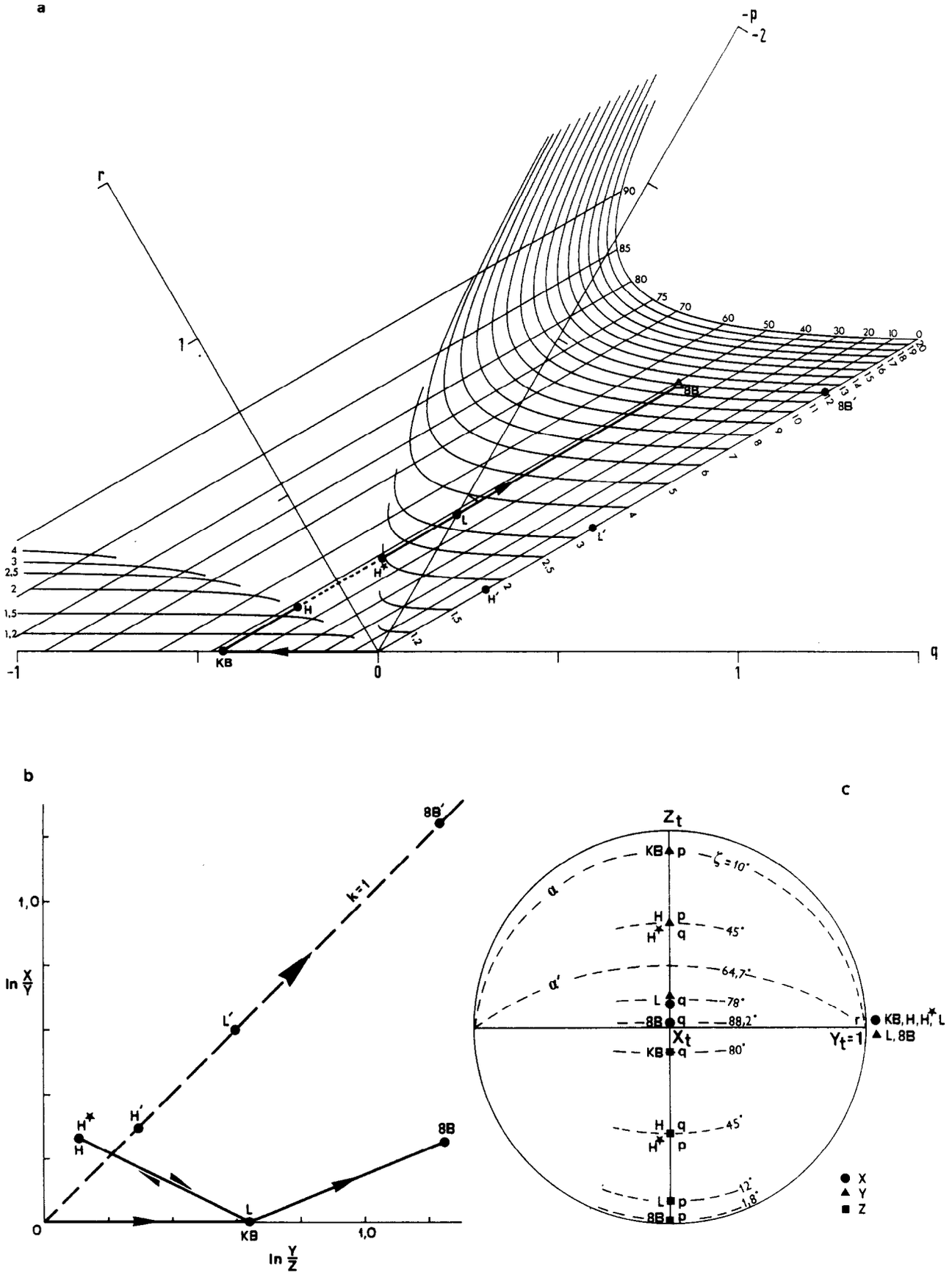

Fig. 23. Obliquely superposed pure shear model for $\zeta = 10°$ (see text for details): (a) three axis planar diagram showing lines of equal compaction and equal pure shear ratio; (b) logarithmic deformation plot; (c) equal-area lower-hemisphere stereoplot.

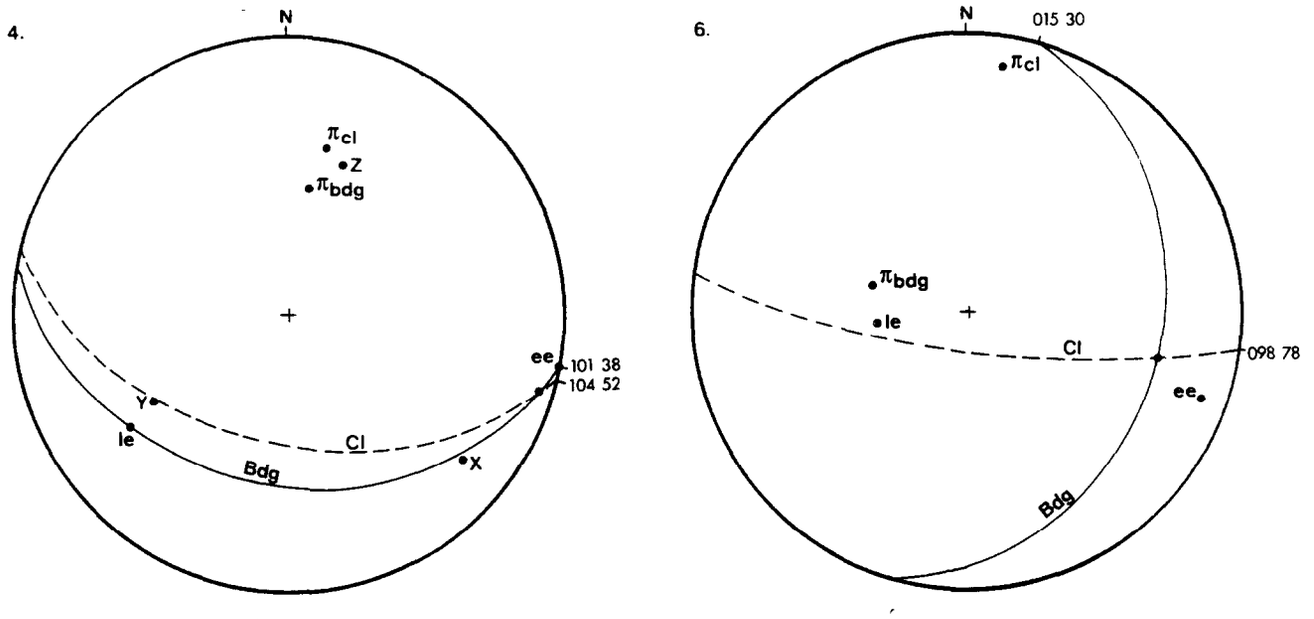

Z	0,59	42	021	bdg/cl	6	107
Y	1,17	42	238	ee (early extension)	0	101
X	1,43	19	129	le (late extension)	29	235

strain unknown	bdg/cl	30	104
	ee	11	110
	le	62	263

Fig. 25. Orientation data for the quartz fibres at sites 4 and 6. Stereoplots are equal-area lower-hemisphere.

bedding and cleavage oblique, one axis of the finite strain ellipsoid parallel to the gently ESE or WNW plunging bedding–cleavage intersection, and the long axis of the finite strain ellipse, in the section perpendicular to the bedding–cleavage intersection, in the imbricate position relative to bedding and cleavage traces. Sites 20, 21 and 22 differ only in the orientation of the bedding–cleavage intersection, which is here rotated counter-clockwise. All these sites could thus possibly be interpreted in terms of the compaction and oblique pure shear model (cf. Fig. 23), if some independent estimate of the amount of initial compaction were known.

Following the principles discussed by Dunnet & Siddans (1971, pp. 313–316), the Rf/ϕ data for the finite strain ellipse and the angle α' between bedding and cleavage traces, should behave coherently via-à-vis the pure shear strain ellipse, in sections normal to the bedding–cleavage intersection. For example, in the case of the site 8B data, if the X_t/Z_t ratio of the tectonic pure shear ($Y_t = 1$, $\zeta = 10°$), was really 12 as discussed above, the bedding trace, now oriented at $\alpha' = 45°$ to cleavage, should originally have been oriented at $\alpha = 86$, i.e. 7° to the future cleavage (Ramsay 1967, eq. 3-34). This does not correspond with a ζ value of 10°. Comparison of the 8B data with the computed compaction and oblique pure shear models, suggest that the bedding trace and total strain ellipse behaviour is most coherent for $\zeta = 10°$ and an initial compaction of 30%. A pure shear with X_t/Z_t ratio of about 8.5 would then more or less produce the observed geometry. This, however, can only be the case for the oblique pure shear model if there was a volume reduction during the tectonic deformation of 30%, producing a stage (vi) shaped ellipsoid with axial ratios $X:Y:Z = 2.07:1.00:0.34$, or if there had been a 15% stretching along the future bedding–cleavage intersection after compaction and prior to the oblique pure shear (see later discussion). Similar conclusions are reached for all the sites listed above.

Incremental strain patterns in the Tinée valley. Although not found at site 8B, there is direct evidence of stretching along the bedding–cleavage intersection early in the tectonic history, followed by later stretching down-dip in the cleavage. This evidence comes from the geometry of syntaxial quartz fibres in cracks, notably in the South Tinée region (sites 4 to 6). Figure 24 shows photomicrographs of such fibres, in section parallel to bedding from site 4. The viewpoint is from above looking down on the bedding surface. Orientation data for the bedding, cleavage and the fibres at sites 4 and 6 are shown stereographically in Fig. 25. The photomicrographs show early fibre development oriented 101° horizontal, with the very earliest increments of stretching having westwards pitches in the bedding. This pattern of curvature, relative to the crack walls, suggests a small amount of opening 101° subhorizontal, then dextral shearing with the shear plane perpendicular to bedding and the shear direction oriented NW–SE in the bedding. The later fibres indicate stretching directions plunging 29° towards 235°, which is almost parallel with the finite Y direction. The geometry of the fibres at site 6 is similar, except that the later stretching directions are in the cleavage. At site 4 the bedding and cleavage planes make small angles with each other.

Compaction–stretching–oblique pure shear model. The effects of post-compactional stretching along the future bedding–cleavage intersection, prior to oblique pure shear ($Y_t = 1$), have been investigated on the three axis

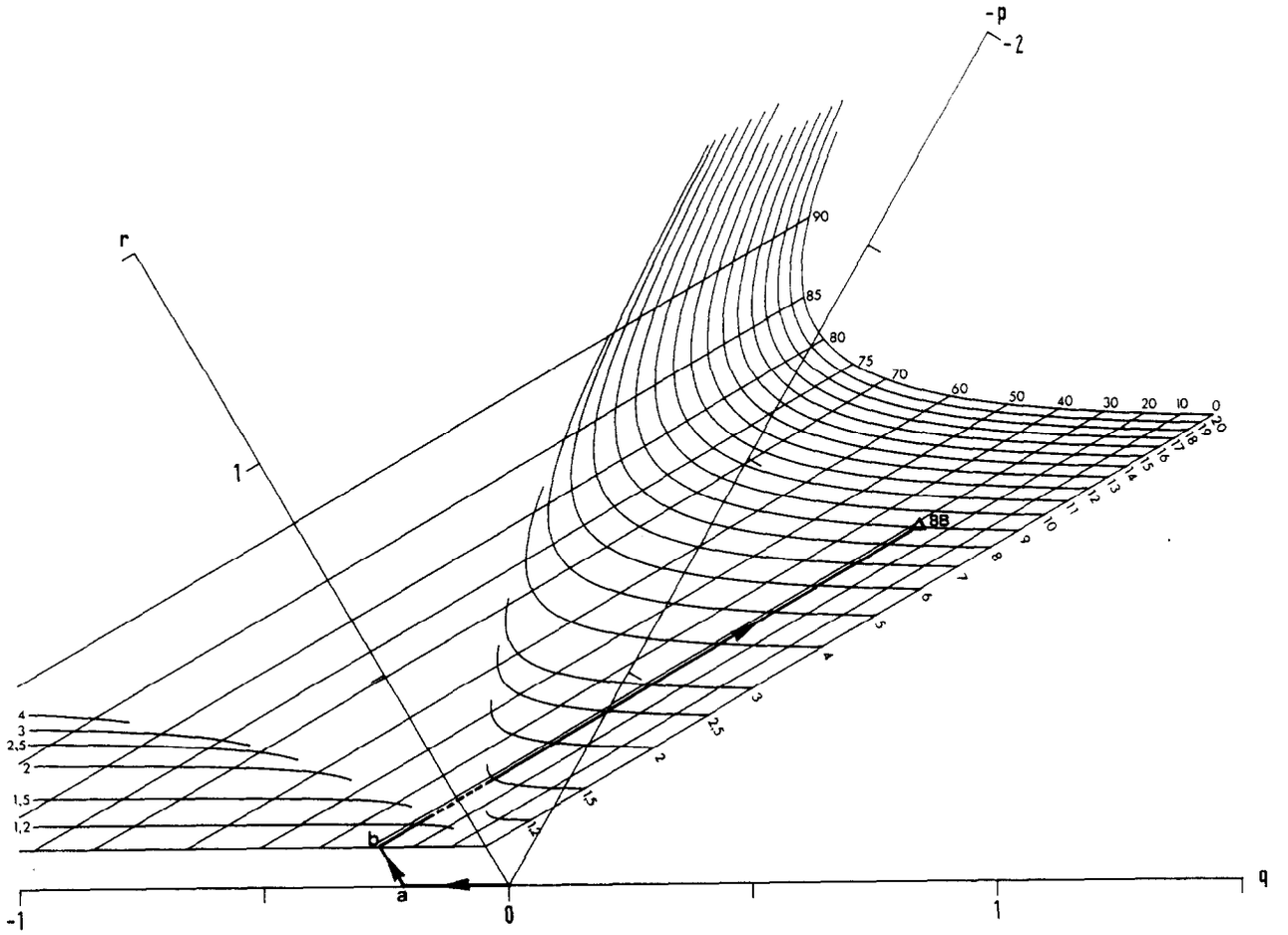

Fig. 26. Three axis planar diagram showing lines of equal compaction and equal pure shear ratio according to the compaction–stretching–oblique pure shear model, for 15% stretching along r and $\zeta = 10°$. See text for details.

diagram. Figure 26 illustrates the effect of a 15% stretching (part a-b of the deformation path), superposed on an initial compaction of 22% by volume loss (part 0-a of the deformation path), then a constant volume, oblique, tectonic pure shear, with $\zeta = 10°$ and $X_t/Z_t = 9$ (part b-8B of the deformation path). Comparison of this figure with Fig. 23(a) shows that the post-compactional stretching has the effect of displacing the grid of equal compaction and equal X_t/Z_t ratios of the pure shear, bodily along the r axis, by an amount equivalent to the logarithmic value of the stretching. The particular example of site 8B, shown in Fig. 26, was found, after much trial and error, to be the best estimate of a deformation path leading to coherent behaviour of the finite strain ellipsoid axial ratio, bedding and cleavage orientations, according to this particular model. The finite strain ellipse evolution, in section perpendicular to the bedding–cleavage intersection, together with the bedding trace evolution, are shown on the pure shear net of Fig. 27. Inspection of this shows that these two reconstructed evolutions are not perfectly coherent: according to the bedding trace orientation, X_t/Z_t associated with the pure shear has a value of 8.1; according to the Rf/ϕ data for the finite strain ellipse, the Rs value is 9. Although this interpretation of the site 8B data is thus imperfect, it is the best compromise estimate that has been obtained by varying the unknown parameters, according to this particular model, and it is a great improvement on the very incoherent pure shear model of Fig. 22.

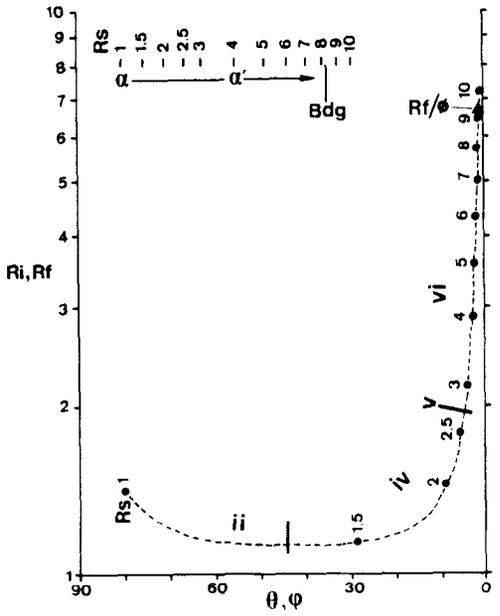

Fig. 27. Evolution of the Rf/ϕ data for the finite strain ellipse and the bedding trace orientation (α), in section normal to the bedding–cleavage intersection, in the case of 22% compaction, 15% stretching along r and oblique pure shear at $\zeta = 10°$.

Table 3. Results of factorization of the finite strain states at eight sites according to the compaction–stretching–oblique pure shear model. Corresponding deformation paths are shown in Fig. 28.

SITE	BEDDING	CLEAVAGE	STAGE	INITIAL COMPACT	INTERMEDIATE EXT Bdg/Cl	PURE SHEAR ζ	X_t	Y_t	Z_t
3	Ø9Ø 24S	275 83N	ii	31%	65%	15	1,1Ø	1,ØØ	Ø,91
8B	314 24NE	3Ø4 59NE	vi	3Ø%	15%	1Ø	3,ØØ	1,ØØ	Ø,33
13	Ø33 2ØSE	284 52N	iv	41%	55%	1Ø	1,92	1,ØØ	Ø,52
17	162 36W	13Ø 2ØNE	iv	3Ø%	95%	15	1,67	1,ØØ	Ø,6Ø
18	Ø97 45S	287 3ØN	iv	4Ø%	5Ø%	1Ø	1,32	1,ØØ	Ø,76
2Ø	Ø7Ø 75SE	2Ø6 34W	iv	25%	55%	1Ø	1,41	1,ØØ	Ø,71
21	249 8ØNW	258 19NW	iv	36%	6Ø%	1Ø	1,77	1,ØØ	Ø,56
22	Ø66 83SE	278 47N	iv	27%	1ØØ%	15	1,66	1,ØØ	Ø,6Ø

Of the previously listed sites that had suitable geometry, with monoclinic symmetry, to attempt this sort of analysis, all except site 1 produced results that are reasonably coherent according to this model. These results are listed in Table 3 and the estimated deformation paths are shown on a three axis diagram in Fig. 28, along with the deformation fields associated with the geographical subregions. In looking at the length of deformation path representing obliquely superposed tectonic pure shear, in Fig. 28, it is important to remember that identical lengths represent different amounts of pure shear, according to the ζ value, and that all deformation paths jump over the region where lines of equal X_t/Z_t ratio are discontinuous. The length of a deformation path depends upon which equal compaction line it follows and the ζ value. Inspection of the pure shear axial ratios in Table 3, however, shows that the general pattern that was previously envisaged: that the North Tinée and Vionène rocks are more highly deformed than the rest, and that the South Daluis and Cians rocks are less deformed or correspond with the lower deformation states seen in the South Tinée region, are generally confirmed. A single difference that appears is that the amount of pure shear suffered by the Roya rocks now partially overlaps the ranges of values for the Cians rocks. An interesting feature of the deformation paths shown in Fig. 28 is that the originally estimated range of initial compaction values, 0–80% according to the orthogonal pure shear model (Fig. 22), is much reduced, since the geometric effect of the post-compactional stretching is to decrease the necessary amount of initial compaction. A less happy result of deformation paths with this form is that rocks whose finite strain ellipsoids have stage (iii) or near-prolate shapes, cannot automatically be attributed to an orthogonal pure shear model, since such shapes can be produced by significant stretching of little compacted rocks.

Of the 25 new sites analysed in this study, 8 can perhaps be explained by the above model. Site 1, which at first sight had suitable geometry, turned out to be disappointing, since no combination of initial compaction, stretching, then oblique pure shear, could get the corresponding point on the three axis diagram out of the theoretically impossible region of discontinuous lines of X_t/Z_t ratio. Site 2 has no visible cleavage, site 8C is in a fold hinge region so represents a range of bedding orientations, and at site 9 the finite X axis is perfectly parallel with cleavage. Sites 7, 11, 12, 14 and 16 have one principal axis of the finite strain ellipsoid subparallel with the bedding–cleavage intersection and tectonically imbricate spots, but the sense of imbrication is wrong relative to the bedding trace orientation, in the section perpendicular to the bedding–cleavage intersection. All other remaining sites showed overall triclinic symmetry,

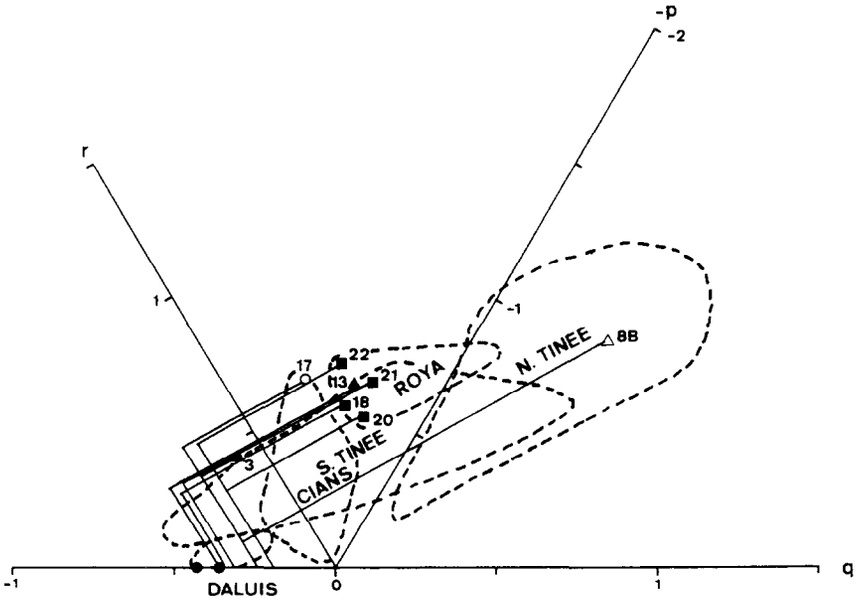

Fig. 28. Three axis planar diagram showing estimated deformation paths, according to the compaction–stretching–oblique pure shear model, for the eight sites listed in Table 3. See text for discussion.

with none of the ellipsoid axes being parallel to the bedding–cleavage intersection. These rocks have so many unknown variables that no factorization into initial compaction and tectonic deformation seems possible. The effects of incremental volume change during tectonic deformation, non-plane strain deformations and non-coaxial superpositions of tectonic strain increments, have not been investigated. Clearly much remains to be done by way of interpretation in this area of abundant finite strain data.

Age of deformation

The existence of pre-Triassic folds in the Roya region and the local field evidence of at least two deformation phases having involved the Permian rocks in the Tinée region and the Dôme de Barrot, have been described in a previous section. The magnitude of the ductile strains, if any, associated with the pre-Triassic events, remains unknown to date (see discussions in Graham 1978b, pp. 221–222; Siddans 1980, pp. 289–291). Since the field relations of the pre-Triassic folds, the Werfenian quartzites and their detached Mesozoic cover are clearest in the Roya region, we renew that discussion there.

The geometry of the pre-Triassic folds in the Série de Capeirotto and of the Alpine folds in the Werfenian quartzites are shown in Figs. 18 and 19. Guillaume & Toussaint (1965) described the two cleavages that are often seen in the pelitic Permian rocks and noted that they are also found in the Upper Werfenian, above the quartzites. They attributed the lack of cleavage in the intervening quartzites (and in the Série du Bego to the north) to the greater competency of these formations. Since both cleavages are found in the Upper Werfenian they must both be of Alpine age.

The compaction–stretching–oblique pure shear model, developed in the previous section, suggested that the tectonic shortening directions were oriented obliquely to bedding in the Permian rocks. The best-fitting angles ζ, for sites 18–22 in the Roya valley, have values in the range 10–15°. These sites are all on the steeply southern dipping, or even overturned, limb of a pre-Triassic fold, where maximum angular unconformity with the overlying quartzites is seen, dihedral angles between poles to bedding in the two formations are up to 75°. Vis-à-vis the Alpine folds, these sites are just to the north of a synclinal hinge. This all corresponds well with the principles of folding of obliquely inclined surfaces into a system of flattened buckle folds, where the initial dihedral angles were small (<40°, see Ramsay 1961, fig. 14, 1967, pp. 498–500), the estimated values of pure shear (Table 3) corresponding with the flattening component, the estimated values of ζ corresponding perhaps with the initial dihedral angles. The pre-Triassic folds then become very gentle structures, with interlimb angles greater than 150° (Fleuty 1964) and with no appreciable ductile deformation associated with their formation (at least not in sections perpendicular to the future bedding–cleavage intersection). All the locally observed ductile deformation features then become Alpine in age.

Relationship with deformation in the crystalline basement

Within the Permian rocks of the southeast end of the Argentera Massif (region of sections b–b to h–h in Figs. 2 and 3), four lithostratigraphic formations are known (Faure-Muret 1955, pp. 159–186): (top) essentially pelitic Série de Capeirotto; essentially psammitic and conglomeratic Série du Bego; essentially pelitic Série de Merveilles; (bottom) essentially psammitic and conglomeratic Série de l'Inferno. The lower two formations are of more restricted geographic extent than the upper two and are wedge-shaped in cross-section.

A very detailed, three-dimensional study, combining borehole data with surface and subsurface mapping, in the region of la Minière de Valauria (region of section e–e in Figs. 2 and 3), was described by Aicard *et al.* (1968). This area is situated towards the NE limit of outcrops of the Unité de Vièvе–Valmasque, the most external tectonic unit in the region. Detailed maps and cross-sections by these authors show quite clearly that:

(1) Thick Permian rocks here occupy a NW–SE trending graben.

(2) Cleavage development in the Série de l'Inferno, in stratigraphic contact with the basement, is strictly related to basement faults: steeply dipping zones of basement cataclasis and retrograde Alpine metamorphism. These basement faults include those that originally controlled Permian sedimentation. Cleavage development in the Permian and basement cataclasis are equally associated with faults that have normal (extension) and reverse (contraction) geometry.

(3) Upwards in the Permian succession cleavage development is more widespread in the Série de Merveilles and Série du Bego.

(4) The Série du Bego is folded, the Série de l'Inferno is not. Disharmony between the two competent formations was enabled by the incompetent Série de Merveilles acting as an accommodation horizon, but not as a wholesale décollement level.

(5) The Werfenian quartzites overstep the Série du Bego onto the Série de Merveilles, the angular unconformity and the quartzites are folded together with the Permian rocks and have a single common cleavage, which is thus of Alpine age.

This model of basement block faulting passing up into folds and widespread cleavage development in the Permian rocks has been extrapolated to the southeast in the cross sections of Fig. 3, and is thought to represent the structure at some depth below the Roya valley.

To the northeast the Unité de Vièvе–Valmasque is overthrust by the Unité de la Rocca dell'Abisso (Figs. 2 and 3). Mesozoic rocks are pinched into a syncline, or a series of folds, below and along the map length of the thrust (see serial sections in Faure-Muret & Fallot 1957, pl. 1; Vernet 1967b, fig. 7). Permian rocks are involved in the displacements, together with crystalline basement, in the upper tectonic unit. To the north and west

this thrust passes into a zone of basement cataclasis that can be followed for some 30 km, traversing first the granite à enclaves de la Valmasque, then the granite de l'Argentera (see Fig. 2). It almost joins up with the faille de Bersezio, demonstrably an Alpine, dextral, strike-slip fault, displacing both the Nappe de flysch à helminthoides and the northern boundary of the basement massif (Sturani 1962, and many subsequent authors listed in Bogdanoff 1980, p. 178). Vernet (1965) showed that the 3 km dextral, strike-slip Alpine displacement was along the plane of an older (Hercynian) mylonite zone in the basement.

Other basement fault zones that involve Mesozoic rocks sometimes have a proven important dextral, strike-slip component, e.g. the Faille de l'Inciano (Sturani 1962, Malaroda *et al.* 1970) in the north, and a series of faults displacing the Permian/basement boundary in the south (Vernet 1979). On the contrary, other basement faults have a proven Alpine displacement with an important contraction component, e.g. the Permian/basement contact just north of Valdeblore (Lemoine 1948) and in the St. Sauveur region (Graham 1978b).

The geometric interpretation of the finite strain pattern seen in the Permian rocks, as developed in the previous section, was in terms of successive:

(1) Diagenetic compaction by volume loss.

(2) Gentle pre-Triassic flexing about NW–SE or WNW–ESE subhorizontal axes, with no appreciable internal deformation.

(3) Subhorizontal NW–SE or WNW–ESE stretching, parallel to the older pre-Triassic axes and the future Alpine bedding–cleavage intersection.

(4) Ductile Alpine deformation, folding and cleavage development, due to a more or less plane strain pure shear, with a tectonic shortening direction NE–SW or NNE–SSW subhorizontal or plunging SW, and subvertical or NE plunging tectonic extension.

This suggests that basement faults with an important Alpine contractional component first had a NW–SE trending, dextral, strike-slip component. The same basement faults have had a long history, probably starting as Hercynian shear zones, they became successively:

(1) Normal faults controlling Permian sedimentation in a regime of crustal extension.

(2) Possibly continuing the same extensional regime they moved to produce the pre-Triassic flexures.

(3) Alpine, dextral strike-slip faults.

(4) Alpine contraction faults in a regime of NE–SW crustal shortening.

In a more regional view of Alpine deformation in this part of the External Zone, the NW–SE dextral, strike-slip basement faulting may correspond with some aspects of the model of Western Alpine evolution proposed by Vialon (1974, see in particular the southeast parts of Fig. 9) and by Boudon *et al.* (1976, see in particular the southeast parts of Fig. 6). The complex zone, Monaco–Sospel–Breil–Saorge, including the gypsiferous diapirs of Sospel and Breil, the NNE–SSW col de Pérus syncline and the NE–SW en-échelon folds and faults of Saorge (see discussion in Lanteaume 1968, pp. 343–344) may represent a complementary NNE–SSW trending, sinistral strike-slip fault in the basement.

The closely spaced depth to basement contours just southwest of the Dôme de Barrot (Fig. 2, contours after Ménard 1980), indicate that the top of the basement dips quite steeply SSW. The existence of the Arc de Castellane to the south (Fig. 1) implies at least basement uplift to the north, according to any gravity driven model to explain the arc, and basement displacement towards the south if the arc is attributed to the 'pushing' effect of the basement. The interpretation by Goguel (1936, pl. 2, section 5), in terms of a contraction fault in the basement just to the southwest of the Dôme de Barrot, is followed in Fig. 3 (section a–a).

The regional pattern of finite strain described in this study is entirely consistent with that already demonstrated by Graham (1978b). An interpretative difference is that we now propose a post-compactional, pre-oblique pure shear, subhorizontal NW–SE or WNW–ESE stretching. As shown by Graham (1978b, fig. 13), in map view finite strain ellipses in the Permian rocks have their long axes oriented NW–SE or WNW–ESE, along a traverse from the Dôme de Barrot to the Argentera Massif. Axial ratios increase from 1 in the western Dôme de Barrot to quite high values near the massif. Vis-à-vis the tectonic pure shear ellipsoid these are more or less Y_tZ_t sections. In vertical section along the same traverse, the maximum extension direction plunges down-dip in the upright or NE dipping cleavage. The magnitude of this extension increases from zero in western parts of the Dôme de Barrot to high values near the massif. At the southeast end of the massif, in the St. Martin–Vésubie–Roya region, the tectonic pure shear ratios are generally lower than the highest values seen in the North Tinée and Vionène region. In map view the strain ellipses here are more E–W oriented, or even locally NE–SW (sites 20 and 21).

Overall we interpret this pattern in terms of NE–SW subhorizontal contraction in the basement, by reverse displacements along reactivated faults. The magnitude of this contraction increases from locally zero in the west Dôme de Barrot, to high values in the Argentera Massif. The rather lower strain values seen in the southeast (Roya region), may be due either to a greater depth to basement there, or to a decreased amount of basement contraction. The locally observed NE–SW finite extension directions (sites 20 and 21) are associated with anomalous palaeomagnetic directions (50–60° anticlockwise rotation). These may be due to local southwest shearing just below the contact with the Werfenian quartzites, or to sinistral, strike-slip displacements along the Monaco–Sospel–Breil–Saorge line.

Acknowledgements—We thank W. H. Owens for providing up to date versions of his programs and for checking out results obtained from our BASIC versions, and R. H. Graham for his always stimulating discussions on the geology of the Alpes Maritimes. Their many helpful comments greatly improved the revised manuscript.

REFERENCES

Aicard, P., Autran, A., Gerard, J. & Lougnon, J. 1968. Sur l'âge tertiaire, syntectonique et synmétamorphique alpin du gisement

plombozincifère de Valauria (Commune de Tende, Alpes Maritimes). *Bull. Bur. Rech. géol. min. Fr.* **1**, 5–14.

Amaudric du Chaffaut, S. & Villey, M. 1979. Une coupe des Alpes de l'Argentera–Mercantour à la zone de Sestri-Voltaggio. *Bull. Soc. géol. Fr.* **21**, 349–378.

Bogdanoff, S. 1980. Analyse structurale dans la partie occidentale de l'Argentera–Mercantour (Alpes Maritimes). Thèse, Univ. de Paris-Sud, Orsay.

Bogdanoff, S. & Schott, J. J. 1977. Etude paléomagnétique et analyse tectonique dans les schistes rouges permiens du Sud de l'Argentera. *Bull. Soc. géol. Fr.* **19**, 909–916.

Bordet, P. 1950. Le dôme permien de Barrot (Alpes Maritimes) et son auréole de terrains secondaires. *Bull. Serv. Carte géol. Fr.* **48**, 51–89.

Boudon, J., Gammond, J. F., Gratier, J. P., Robert, J. P., Depardon, J. P., Gay, M., Ruhland, M. & Vialon, P. 1976. L'arc alpin occidental: réorientation de structures primitivement E–W par glissement et étirement dans un système de compression global N–S? *Eclog. geol. Helv.* **69**, 509–519.

Breddin, H. 1956. Die tektonische Deformation der Fossilien im Rheinischen Schiefergebirge. *Z. deutsch geol. Ges.* **106**, 227–305.

Campredon, R. & Boucarut, M. 1975. *Alpes-Maritimes, Maures, Esterel. Guides géologiques régionaux*. Masson & Cie, Paris.

Cobbold, P. R. 1979. Removal of finite deformation using strain trajectories. *J. Struct. Geol.* **1**, 67–72.

Cobbold, P. R. & Percevault, M. N. 1983. Spatial integration of strain using finite elements. *J. Struct Geol.* **5**, 299–305.

Debelmas, J. 1974. *Géologie de la France*, 2, Doin, Paris.

Dunnet, D. 1969. A technique of finite strain analysis using elliptical particles. *Tectonophysics* **7**, 117–136.

Dunnet, D. & Siddans, A. W. B. 1971. Non-random sedimentary fabrics and their modification by strain. *Tectonophysics* **12**, 307–325.

Faure-Muret, A. 1947. Sur des affleurements de Trias pincés dans les schistes cristallins de la vallée de la Tinée. *C.r. hebd. Séanc. Acad. Sci., Paris* **224**, 205–207.

Faure-Muret, A. 1948. Tectonique alpine et tectonique anté-triasique au nord-ouest du massif de l'Argentera–Mercantour (Alpes Maritimes). *C.r. hebd. Séanc. Acad. Sci., Paris* **226**, 1025–1027.

Faure-Muret, A. 1955. Etudes géologiques sur le massif de l'Argentera–Mercantour et ses enveloppes sédimentaires. *Mém Serv. Carte géol. dét. Fr.*

Faure-Muret, A. & Fallot, P. 1957. Feuilles de Boréon, Vièvе, Saint-Martin-Vésubie et Tende au 50.000^{e}. Liaisons tectoniques et stratigraphiques. *Bull. Serv. Carte géol. Fr.* **55**, 189–198.

Fleuty, M. J. 1964. The description of folds. *Proc. Geol. Ass.* **75**, 461–492.

Fry, N. 1979. Random point distributions and strain measurements in rocks. *Tectonophysics* **60**, 89–105.

Goguel, J. 1932. Description géologique du Luberon. *Bull. Serv. Carte géol. Fr.* **36**, 1–74.

Goguel, J. 1933. Revision de la feuille de Forcalquier. *Bull. Serv. Carte géol. Fr.* **38**, 129–158.

Goguel, J. 1936. Description tectonique de la bordure des Alpes de la Bléone au Var. *Mém Serv. Carte géol. dét. Fr.*

Graham, R. H. 1978a. Wrench faults, arcuate fold patterns and deformation in the southern French Alps. *Proc. Geol. Ass.* **89**, 125–142.

Graham, R. H. 1978b. Quantitative deformation studies in the Permian rocks of Alpes-Maritimes. *Mém. Bur. Rech. géol. min. Fr.* **91**, 219–238.

Graham, R. H. 1981. Gravity sliding in the Maritime Alps. In: *Thrust and Nappe Tectonics* (edited by McClay, K. & Price, N. J.). *Spec. Publs. geol. Soc. Lond.* **9**, 335–352.

Guillaume, A. & Toussaint, J. F. 1965. Précisions stratigraphiques et microstructurales sur le Permien et le Trias basal de la Haute vallée de la Roya (massif de l'Argentera, Alpes Maritimes). *C.r. hebd. Séanc. Acad. Sci., Paris* **261**, 4159–4161.

Hanna, S. S. & Fry, N. 1979. A comparison of methods of strain determination in rocks from southwest Dyfed (Pembrokeshire) and adjacent areas. *J. Struct. Geol.* **1**, 155–162.

Henry, B. 1971. Contribution à l'étude structurale du Dôme de Barrot: microtectonique, anisotropie de susceptibilité magnétique et paléomagnétisme. Thèse 3eme cycle, Univ. de Paris.

Henry, B. 1973. Studies of microstructures, anisotropy of magnetic susceptibility and palaeomagnetism of the Permian Dôme de Barrot (France): palaeotectonic and palaeosedimentological implications. *Tectonophysics* **17**, 61–72.

Hrouda, F. & Stephenson, A. in press. On the standardization of magnetic susceptibility measurements. *Phys. Earth Planet. Inter.*

Horrenberger, J. C., Michard, A. & Werner, P. 1978. Le couloir de décrochement de Bersezio en Haute Stura, Alpes externes, Italie. Structure de compression subméridienne. *Bull. Sci. Géol.* **31**, 15–20.

Kligfield, R., Owens, W. H. & Lowrie, W. 1981a. Magnetic susceptibility anisotropy, strain and progressive deformation in Permian sediments from the Maritime Alps (France). *Earth Planet. Sci. Lett.* **55**, 181–189.

Kligfield, R., Carmignani, L. & Owens, W. H. 1981b. Strain analysis of a Northern Apennine shear zone using deformed marble breccias. *J. Struct. Geol.* **3**, 421–436.

Kligfield, R., Lowrie, W., Hirt, A. & Siddans, A. W. B. 1983. Effect of progressive deformation on remanent magnetization of Permian redbeds from the Alpes Maritimes (France). *Tectonophysics* **97**, 59–85.

Lanteaume, M. 1968. Contribution à l'étude géologique des Alpes Maritimes Franco-Italiennes. *Mém Serv. Carte géol. dét. Fr.*

Lemoine, M. 1948. Sur des dislocations de la bordure du massif de l'Argentera–Mercantour au nord de Valdeblore (Alpes-Maritimes). *C.r. hebd. Séanc. Acad. Sci., Paris* **226**, 1027–1029.

Malaroda, R., Carraro, F., Dal Piaz, G. V., Franceschetti, B., Sturani, C. & Zanella, E. 1970. Carta geologica del massiccio dell'Argentera alla scale 1:50,000 e note illustrative. *Mem. Soc. Geol. It.* **9**, 557–663.

Ménard, G. 1980. Profondeur du socle antétriasique dans le sud-est de la France. *C.r. hebd. Séanc. Acad. Sci., Paris* **290**, 299–302.

Owens, W. H. 1974. Representation of finite strain-state by three-axis planar diagrams. *Bull. geol. Soc. Am.* **85**, 307–310.

Owens, W. H. in press. The calculation of a best-fit ellipsoid from elliptical sections on arbitrary planes. *J. Struct. Geol.*

Ramsay, J. G. 1961. The effects of folding on the orientation of sedimentation structures. *J. Geol.* **69**, 84–100.

Ramsay, J. G. 1967. *Folding and Fracturing of Rocks*. McGraw-Hill, New York.

Ramsay, J. G. & Huber, M. in press. *Techniques of Modern Structural Geology*. Academic Press, London.

Rathore, J. S. 1979. Magnetic susceptibility anisotropy in the Cambrian slate belt of North Wales and correlation with strain. *Tectonophysics* **24**, 115–136.

Shimamoto, T. & Ikeda, Y. 1976. A simple algebraic method for strain estimation from deformed ellipsoidal objects.—1. Basic theory. *Tectonophysics* **36**, 315–337.

Siddans, A. W. B. 1979. Arcuate fold and thrust patterns in the subalpine chains of southeast France. *J. Struct. Geol.* **1**, 117–126.

Siddans, A. W. B. 1980. Compaction, métamorphisme et structurologie des argilites permiennes dans les Alpes-Maritimes (France). *Revue Géogr. phys. Géol. dyn.* **22**, 279–292.

Sturani, C. 1962. Il complesso sedimentario autoctono all'estremo nord-occidentale dell Massiccio dell'Argentera. *Mem. Ist. Geol. Min. Univ. Padova.*

Sturani, C. 1967. Guida alle Excursioni del 64° Congresso della Soc. Geol. Ital. Torino-Cuneo-Massiccio dell'Argentera, 10–16 Sept. '67. Pacini Mariotti, Pisa.

Van den Ende, C. 1970. Secular variation in the Permian redbeds of the Dôme de Barrot (S. France). In: *Palaeogeophysics* (edited by Runcorn, S. K.). Academic Press, London, 101–116.

Van den Ende, C. 1977. Paleomagnetism of Permian redbeds of the Dôme de Barrot (S. France). Unpublished Ph.D. thesis, University of Utrecht.

Vaslet, D. 1978. Analyse structurale de la terminaison sud-orientale du massif de l'Argentera–Mercantour. Thèse 3eme cycle, Univ. de Caen.

Vaslet, D., Lanteaume, M., Campredon, R. & Gigot, P. 1977. Rôle et importance des chevauchements impliquant le socle et la couverture à la terminaison SE du massif de l'Argentera–Mercantour (Alpes Maritimes). 5eme *R.A.S.T.*, Rennes.

Vernet, J. 1965. Sur un décrochement tardif horizontal du socle dans la région méridionale de la zone des Massifs cristallins externes (Massif de l'Argentera, Alpes-Maritimes). *C.r. hebd. Séanc. Acad. Sci., Paris* **261**, 1358–1360.

Vernet, J. 1967a. Le massif de l'Argentera. *Trav. Lab. géol. Grenoble* **43**, 193–216.

Vernet, J. 1967b. Données récentes sur la tectonique du Massif de l'Argentera. *Trav. Lab. géol. Grenoble* **43**, 217–247.

Vernet, J. 1979. Sur un accident profond de coulissement d'âge néogène dans les Alpes occidentales. *C.r. hebd. Séanc. Acad. Sci., Paris* **289**, 61–64.

Vialon, P. 1974. Les déformations "synschisteuses" superposées en Dauphiné. Leur place dans la collision des éléments du socle pré-alpin. Conséquences pétrostructurales. *Bull. Suisse de Min. et Pétrogr.* **54**, 663–690.

Zijderveld, J. D. A. 1975. Paleomagnetism of the Esterel rocks. Unpublished Ph.D. thesis, University of Utrecht.